CORSO ALAIN JODY

NANOSTRUCTURED OPTICAL COATINGS FOR SOLAR PHYSICS OBSERVATIONS FROM SPACE

TESI DI LAUREA

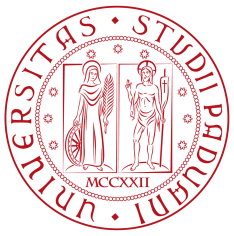

Relatore: Prof.sa Pelizzo Maria Guglielmina
Co-relatore: Dott. Suman Michele
Co-relatore: Dott.sa Zuppella Paola
Università di Padova
Facoltà di Ingegneria
Laurea Specialistica in Ingegneria Elettronica
Luglio 2010

Ai miei nonni
che avrebbero voluto esserci in questo giorno,
ai miei cari genitori
e alla mia Valentina

ABSTRACT

METIS is a coronagraph onboard of Solar Orbiter. It will perform simultaneous observation at HeII Lyman-α line, HI Lyman-α line and in visible. To achieve such capability, instrument mirrors need to be coated by multilayer structures with high efficiency at all three spectral ranges.

Coatings with higher performances respect than standard coating based on Mo/Si couple are desirable. SCORE, an instrument prototype of METIS, has just flown on board of a NASA sounding rocket: in this case, optics were coated with Mg/SiC couple. Better performances have been obtained in term of reflectivity, but long term stability of this coating is an open problem. Moreover the harsh conditions of the environment met during the Solar Orbiter mission given by plasma particles and high temperature could affect the lifetime of the optical components on the long term.

We present the design and reflectivity tests of new multilayer structure in which performances improvement is obtained by the use of novel capping layers. All multilayers are tuned at 30.4nm line but the design also maximize the performances at 121.6nm and 500 - 650 nm visible range. Analysis of Solar Orbiter environment have been carried on in order to point out the main damaging sources for the nanostructures. Experimental tests for investigating the effects of the thermal heating and particles bombardments in the reflectivity performances have been planned.

ACKNOWLEDGEMENTS

Un sentito ringraziamento a tutti coloro che in questi anni mi hanno aiutato ad affrontare il peso dello studio. Un Grazie particolare ai miei genitori che mi hanno sostenuto in tutti questi anni di studio. Un grazie anche a Valentina, la mia dolce metà, senza la quale non sarei mai diventato la persona che sono ora. Un dolce ricordo anche ai miei nonni che avrebbero voluto essere qui in questi giorni di festa.

Un grazie alla Prof.sa Maria Guglielmina Pelizzo per il sostegno e gli utili consigli ottenuti durante il periodo di tesi presso il laboratorio LUXOR di Padova. Un Grazie ai miei due co-relatori, Dott. Michele Suman e Dott.sa Paola Zuppela per l'aiuto e le innumerevoli conversazioni tecniche (e non ...) svolte in questi mesi di lavoro. Un Grazie anche al Dott. Gianni Monaco per i suoi preziosi suggerimenti e per la sua indispensabile competenza presso il Sinclotrone di Trieste e nell'analisi AFM dei campioni depositati.

Infine un grazie a tutti i miei amici che mi sono sempre stati vicini fino a questo momento, sperando che anche per loro arrivi questo importante momento di gioia.

Padova, luglio 2010 Corso Alain Jody

CONTENTS

LIST OF FIGURES

LIST OF TABLES

INTRODUCTION

We live in the extended atmosphere of an active star. While sunlight enables and sustains life, the Sun's variability produces streams of high-energy particles and radiation that can affect life. Everyone is familiar with changes in the weather on Earth, but "weather" also occurs in space. Just as it drives weather on Earth, the Sun is responsible for disturbances in our space environment. Many space missions are dedicated for understanding the changing of Sun and its effects on the Solar System, life, and society.

The European Space Agency (ESA) foresees a new spacecraft, the Solar Orbiter, which is going to be launched in January 2017 or July 2018 and will approach our star at the closest distance ever reached before. The Italian Space Agency (ASI) will contribute with the realisation of one of the instrument on board: the METIS EUV-UV-VIS Coronagraph, devoted to the imaging/spectroscopy of the extended Corona.

Inside this project the CNR-IFN LUXOR laboratory in Padova (Italy) is responsible for the design and test of the multilayer optical coatings for the primary, secondary mirrors and grating of this instrument. Such coatings consist in a stack of thin films deposited on the optics substrates characterised by a thickness in the nanometric scale. Their realisation is technologically challenging, especially considering the harsh environment in which they need to survive for many years.

Design, realisation and tests of new multilayer coatings for METIS instrument have been carried on and here presented. A short description of the mission and on board instruments is reported; a detailed analysis of the Solar Orbiter environment has been considered in order to identify the main damaging sources for the optical coatings (Chapter 1). The description of the optical layout of METIS (Chapter 2) and the theory of multilayer (Chapter 3) lead the design of six different kinds of multilayers (Chapter 4). A test plan has been scheduled; first reflectivity tests carried on at ELETTRA synchrotron facility and at LUXOR are presented (Chapter 5). Finally, a discussion on experimental results and future activities is reported (Chapter 6).

1 THE SOLAR ORBITER MISSION AND ITS ENVIRONMENT

Since the beginning of the 1990's six unprecedented spacecraft built in Europe for the Ulysses, SOHO and Cluster missions have made many amazing discoveries about the Sun, and how its storms affect the Earth. Yet, scientists still cannot predict the unruly behaviour of the star on which our lives depend. A closer look at the Sun is required and for this reason ESA has planned the Solar Orbiter Mission [7]: its particular requirements and its environmental characteristics make this project a very useful example for investigating the design and validate procedures of new optical multilayer coatings for solar physics observation from the space.

1.1 WHAT IS SOLAR ORBITER?

Solar Orbiter (also named SOLO) is a Sun-observing satellite that will be launched around the Sun in January 2017 or July 2018 and it will reach the closest distance ever reached by the Sun: during the mission, the spacecraft and its instruments will reach a distance less than one quarter of the Earth's distance from the Sun (as shown in Figure 1).

At this distance, the sunlight will be twenty times more intense then to Earth distances, the spacecraft must bear the inhospitable environment caused by solar wind plasma and powerful bursts of atomic particles from explosions in the solar atmosphere but the technological effort required for successful mission will come in the form of sharp images obtained together with unprecedented measurements of the local near-Sun phenomena. The pictures of the weird solar landscapes, where glowing gas dances and forms loops in the strong magnetic field, will be stunning. They will show details down to 200 kilometers wide, with a tiny fraction of the width of the Sun's visible disc, 1.4 million kilometers.

Solar Orbiter scientific goals

The principal scientific goals of the Solar Orbiter are:

- to determine in-situ the properties and dynamics of plasma, fields and particles in the near-Sun heliosphere;

Figure 1: A pictorial representation of Solar Orbiter spacecraft

- to survey the fine detail of the Sun's magnetized atmosphere;
- to identify the links between activity on the Sun's surface and the resulting evolution of the corona and inner heliosphere, using solar co-rotation passes;
- to observe and characterize the Sun's polar regions and equatorial corona from high latitudes.

From this mission, the scientific community hopes to understand how the solar wind is propelled, how the magnetic fields are generated, how we can predict the solar eruptions and their intensity or if it is possible making long-term forecasts of solar activity.

1.2 SOLAR ORBITER PAYLOAD

Into a mass of 180 kilograms, the scientists want to accommodate a set of in-situ and a set of remote sensing instruments [8]. The payload is protected from the direct solar radiation by

a thermal shield which also ensure a low operating temperature in the spacecraft's systems.

In-situ instruments

The in-situ instruments consist of detectors for observing particles and events in the immediate vicinity of the spacecraft: the charged particles and magnetic fields of the solar wind, radio and magnetic waves in the solar wind, and energetic charged particles flung out by the Sun. The in-situ instruments planned in Solar Orbiter and shown in Figure 2 are:

- **Energetic Particle Detector (EPD)** which will measure the properties of suprathermal and energetic particles. Scientific topics to be addressed include the sources, acceleration mechanisms, and transport processes of these particles.
- **Suprathermal Ion Spectrograph (part of EPD)** which will measure energetic particles ejected from the Sun. Data will be compared to other solar and interplanetary processes to understand solar system space weather. Understanding the connections between the Sun and its planets will allow better prediction on the impacts of solar activity on humans, technological systems and even the presence of life itself in the universe.
- **The Radio and Plasma Waves experiment (RPWE)** is unique amongst the Solar Orbiter instruments in which it makes both in-situ and remote-sensing measurements. RPW will measure magnetic and electric fields at high time resolution using a number of sensors/antennas, to determine the characteristics of electromagnetic and electrostatic waves in the solar wind.
- **The magnetometer (MAG)** will provide in-situ measurements of the heliospheric magnetic field. This will facilitate detailed studies into the way the Sun's magnetic field links into space and evolves over the solar cycle; how particles are accelerated and propagate around the solar system, including to the Earth; how the corona and solar wind are heated and accelerated.
- **Solar Wind Plasma Analyser (SWA)** will consist of a suite of sensors that will measure the density, velocity, and temperature of solar wind ions and electrons, thereby characterising the solar wind between 0.22 and 1.4 AU from the Sun. In addition to determining the bulk properties of the wind, SWA will provide measurements of solar wind ion composition for key elements (e.g. the C, N, O group and Fe, Si or Mg).

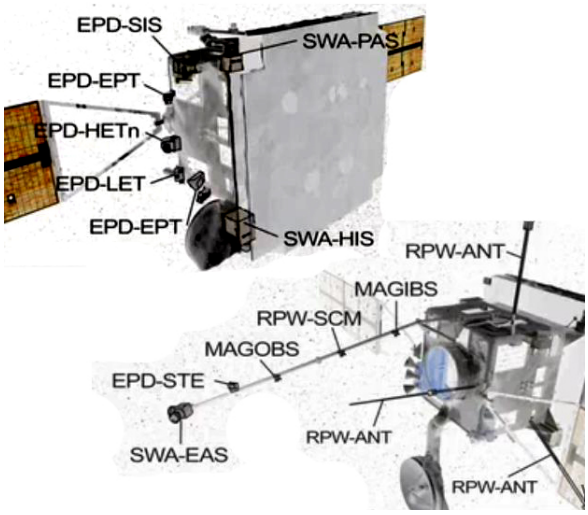

Figure 2: In-situ instruments on Solar Orbiter spacecraft.

Remote sensing instruments

The remote sensing instruments will observe the Sun's surface and atmosphere: for observing the Sun, these kind of instruments require an opening in thermal shield and this is a delicate point in the design processes. The gas of the atmosphere is best seen by its strong emissions of short-wavelength ultraviolet rays. Tuned to these will be a full-Sun and high-resolution imager and a high-resolution spectrometer. The outer atmosphere will be revealed by ultraviolet and visible-light coronagraphs that blot out the bright disc of the Sun. To examine the surface by visible light, and measure local magnetic fields, Solar Orbiter will carry a high-resolution telescope and magnetograph. The remote sensing instruments planed for Solar Orbiter and shown in Figure 3 are:

- **Extreme Ultraviolet Imager (EUI)** which will provide image sequences of the solar atmospheric layers above the photosphere, thereby providing an indispensable link between the solar surface and outer corona that ultimately shapes the characteristics of the interplanetary medium. EUI will also provide the first-ever images of the Sun from an out-of-ecliptic viewpoint (up to 34° of solar latitude during the extended mission phase).

- **Coronagraph (METIS/COR)** which will simultaneously image the visible and ultraviolet emission of the solar corona and diagnose, with unprecedented temporal coverage and spatial resolution, the structure and dynamics of the full corona in the range from 1.2 to 3.0 (from 1.6 to 4.1) solar radii from Sun centre, at minimum (maximum) perihelion

during the nominal mission. This is a region that is crucial in linking the solar atmospheric phenomena to their evolution in the inner heliosphere.

- **The visible imager and magnetograph (PHI)** which will provide high-resolution and full-disk measurements of the photospheric vector magnetic field and line-of-sight (LOS) velocity as well as the continuum intensity in the visible wavelength range. The LOS velocity maps will have the accuracy and stability to allow detailed helioseismic investigations of the solar interior, in particular of the solar convection zone.

- **Heliospheric Imager (SoloHI)** which will provide revolutionary measurements to pinpoint coronal mass ejections or CMEs. CMEs are violent eruptions with masses greater than a few billion tons. They travel from 100 to more than 3000 kilometres per second. They have been compared to hurricanes because of the widespread disruption of communications and power systems they can cause when directed at Earth.

- **EUV Spectrometer (SPICE)** which will provide an extreme ultraviolet spectrometer or optical instrument that will measure different wavelengths of light emitted from the sun. Data will advance our understanding of the various dynamics of the sun to better understand the affects on Earth and the solar system.

- **X-ray Imager (STIX)** which will provide imaging spectroscopy of solar thermal and non-thermal X-ray emission. STIX will provide quantitative information on the timing, location, intensity, and spectra of accelerated electrons as well as of high temperature thermal plasmas, mostly associated with flares and/or microflares.

We underline that in this thesis we will considering, as example, the design aspects of optical multilayer coatings intended to METIS.

1.3 MISSION DESCRIPTION

In the currently foreseen scenario, the date of launch is January 2017 or July 2018 when the spacecraft will begin its journey to the Sun lasting approximately 3.4 years. During the journey, the spacecraft will use a series of gravity assists from Venus and

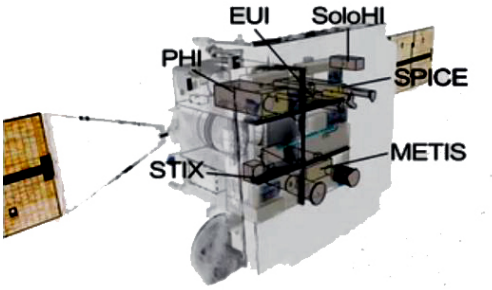

Figure 3: Remote sensing instruments on Solar Orbiter spacecraft.

the Earth for putting Solar Orbiter into a 150-day-long elliptical solar orbit from which it can begin its scientific mission: in the cruise phase is also planed the check and calibration of the payload which will already be able to provide first valuable science data. Upon entering the science orbit, closer encounters to the Sun will be achieved, with perihelion as low as 0.23 AU.

Ground controllers will repeatedly fly Solar Orbiter close to Venus, and use the planet's gravity to nudge the spacecraft into higher inclination orbits. This will enable the instruments to see the polar regions of the Sun clearly for the first time. This is one of the prime scientific goals of the project. After 7.4 years, Solar Orbiter will view the poles from solar latitudes higher than 30°, compared with 7° at best from the Earth.

The total duration of the mission is 9.9 years for the case of launch in 2017 and 8.9 years for the launch in 2018.

1.4 ENVIRONMENTAL ASPECTS

When a space instrument is designed, the effects of the space environment should be studied and considered in the design process. In general, when assessing the effects of the space environment on an instrument, the following aspects should be included:

Solar Orbiter environmental components

- Solar and Planetary Electromagnetic Radiation;
- Neutral Atmosphere;
- Solar Wind;
- Energetic Particle Radiation;
- Particulates;
- Contamination;

- Thermal;

Depending on the characteristics of the mission or the analysis, some of this aspects can be neglected because their contribution is not relevant. For example, when we design an instrument for an interplanetary mission, we can neglect Neutral Atmosphere effects or, for Solar Orbiter, the Planetary Electromagnetic Radiation can be neglected as well.

In our analysis, we want consider only the effects that could change the optical properties of the multilayer mirrors inside an UV-range instrument. In particular, for a multilayer coating which works in the range of the heliospheric distances of Solar Orbiter, it is important to consider the effects induced by Solar flux thermal irradiation, Solar Wind Plasma and Energetic Particles but it is adequate to consider negligible the effects of the other environmental features because their concentration is very small.

1.5 ENVIRONMENTAL CONSTANTS DERIVATION

Many parameters of the mission's environment can not be available for the range of heliospheric distances of Solar Orbiter but only for the distance of the Earth (1AU): in these cases an appropriate estimation method must be applied.

In first analysis, we can consider that many parameters of the environment are strongly dependent on the heliospheric distance and they propagate radially in the space. With this assumption, we can define the corrective parameter

Inverse square law

$$\gamma = \frac{1}{r^2} \tag{1.1}$$

witch provides, in first approximation, a reasonable estimation by multiplying it with the solar constants measured at the Earth distance; this method is named inverse square law.

Sometimes, the best analysis requires to consider the minimum distance from the Sun (e.g. thermal analysis) while other times it is more convenient to consider an average distance (e.g. total protons dose). In Table 1 we have computed, for different launch dates (therefore, different orbital trajectory), the useful scaling factors γ.

Unfortunately, the solar constants are difficult to estimate also at 1AU because the phenomena which generates them is complex and not yet fully understood. However, from experimental measures, we can build a statistical model for computing the

		Radius [AU]	Factor γ
Launch in 2017	Min perihelion	0,23	18,90
	Mission average	0,59	2,87
Launch in 2018	Min perihelion	0,24	17,36
	Mission average	0,59	2,87

Table 1: Scaling factor computed with inverse square law for different launch date

mean values of the solar constants. ESA has released a report in which we find the constants and models useful to estimate the environmental parameters of our interest [9].

1.6 THERMAL ENVIRONMENT

In the Solar Orbiter mission, the spacecraft will reach distances very close from the Sun where the solar irradiance will be very powerful. A thermal shield is planned for protecting the components and instruments during the mission. However, in the thermal shield are planned holes which are used from remote sensing instruments during the observation phases. From these holes the solar irradiance may heats dangerously the interior of the spacecraft and so a thermal analysis should be performed.

Knowing the average solar irradiance at 1AU (Earth), we can estimate the irradiance at perihelion using the inverse square law: we will have a flux approximately $25000 W/m^2$. At perihelion, we will have also the highest working temperature for the spacecraft: these parameters should be used for evaluating the thermal effects in the components of the instruments. The maximum temperature reached to each components depends to the diameter of the opening in the thermal shield and the geometry of the envelope. The general specifications provided by [8] suggest, as project requirements, the maximum temperatures of each components or instruments.

1.7 THE SOLAR WIND

The solar wind is part of the Corona, the Sun's outer atmosphere. The high temperature of the plasma near the sun causes

it to expand outwards against gravity, carrying the solar magnetic field along with it. The solar wind starts at the Sun as a hot dense, slowly moving plasma, but accelerates outwards to become cool, rare and supersonic at the Solar Orbiter perihelion and beyond.

Most of the solar wind's acceleration takes place near the sun and so the Solar Orbiter will not observe significant difference in velocity as its distance from the Sun varies. The solar wind velocity typically lies in the range 300-1200km/s. It is most commonly the slow-speed component, named slow solar wind, with velocities around 400km/s but there are frequent high-speed component, named fast solar wind, with velocities around 700km/s.

Solar wind plasma description

More severe but less frequent disturbances in the solar wind can be caused by coronal mass ejections. In the solar wind, in addition to protons, we can find many ions like He^{++}, O^{6+}, Fe^{10+}. Typically, the kinetic energy for protons is about 1keV while for He^{++} is about 4keV. Other heavy ions can be found in the solar wind although much less concentrated. Again, in order to obtain a reasonable analysis model, it is convenient consider the mean values for the solar wind and its mean composition. From [9] we have the data reported in Table 2.

	At 1Au	Mission average
Density (cm^{-3})	8,7	25
Speed ($\frac{km}{s}$)	468	468
$\frac{N_{alpha}}{N_{proton}}$	0,047	0,047
$\frac{N_{O6+}}{N_{proton}}$	0,0003	0,0003
$\frac{N_{Fe10+}}{N_{proton}}$	$8,77 \cdot 10^{-6}$	$8,77 \cdot 10^{-6}$

Table 2: Characteristic of the plasma in solar wind

In bombardments tests is important consider the total absorbed dose and the particle's energy. For a reasonable estimation, we consider the mean density and speed deduced by inverse square law at mean heliospheric distance. Assuming a duration of the mission around 3500 days, the total protons dose is around $354 \cdot 10^{15} cm^{-2}$.

1.8 ENERGETIC PARTICLES

Energetic charged particles, which can penetrate outer surfaces of spacecraft, are encountered throughout the Solar Orbiter mission, and the effects on the different components should to be considered. The energy for electrons is typically above 100keV, while for protons and other ions this is above 1MeV: in our consideration, also neutrons, gamma-rays and X-rays are considered energetic particles.

Energetic Solar Eruptions

For Solar Orbiter, the main source of these particles is the Energetic Solar Eruptions (ESE). Energetic ions lose energy rapidly in materials, mainly through ionization, and this energy transfer can disrupt or damage targets. Apart from ionizing process, particles can lose energy also through non-ionizing interactions causing "displacement damage" or "bulk damage", where atoms are displaced from their original sites. This can alter the electrical, mechanical or optical properties of materials and is an important damage mechanism for our optical components.

Solar particle events, because of their unpredictability and large variability in magnitude, must be treated statistically. However, large events are confined to a 7-year period defined as solar maximum. Although large events are absent during the remaining 4 solar minimum years of the 11-year solar cycle the occasional small event can still occur. To investigate the effects of these particles (protons and heavy ions) in the multilayer mirrors, we consider again the total absorbed dose: the reference model of time-integrated effects is EPS [9] and it is also available in [10]. For example, in Figure 4 we can see the proton fluence for different energies predicted for different launch dates.

Cosmic-ray ions

Another source of height energetic particle is a continuous flux of galactic cosmic-ray ions. Although the flux is low (a few particles /cm2/sec), cosmic rays include energetic heavy ions which can deposit significant amounts of energy in sensitive volumes and so cause problems. However, during the mission phases, the remote instruments is always directed towards the Sun and the galactic cosmic-ray ions will have not relevant effects in the coated mirrors.

Energetic electrons

Also the energetic electrons should be considered. The energetic electron environment encountered by the Solar Orbiter is dominated by two sources. During solar quiet periods, the majority of high-energy (>100keV) are of Jovian origin, while at solar active periods, it is the solar electrons that are by far the dominating source. The principal effects produced by these electrons are thermal and they can be considered as an additional source in thermal analysis of the optical multilayer coatings.

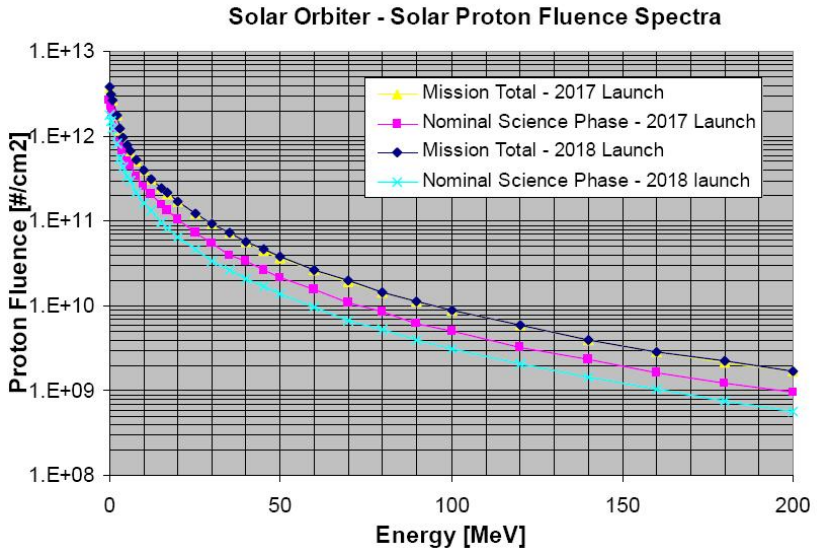

Figure 4: Solar Proton Spectrum for the mission.

2 METIS: THE CORONAGRAPH ON BOARD OF SOLAR ORBITER

METIS, the Multi Element Telescope for Imaging and Spectroscopy, is an instrument proposed to ESA for being part of the payload in Solar Orbiter Mission.
This instrument implements a coronagraph which images the annular corona between 1.3 and 3 solar radii at minimum perihelion; it will observe the HeII Lyman-α line at 30.4nm, the HI Lyman-α line at 121.6nm and the visible wavelengths from 500 to 650nm.
In addition, an EUV/UV spectroscopic channel is implemented without required substantial changes in the base structure because the main optical components are shared with the coronagraph channel.
The principal mirrors, for reflecting the EUV wavelengths, require multilayer coatings which must be optimized also for reflecting UV and visible light.

SCORE

First optical configuration was based on off-axis Gregorian telescope with external occulter and it was investigated in the design of SCORE, the sounding rocket version of METIS[1], launched during HERSCHEL program. The flight of SCORE has showed that effectively a single telescope can observe simultaneously the emission of the outer corona in HeII, HI and visible lines and it has provided first images at these wavelengths.

However, METIS is a remote sensing instruments and it will observe the corona through an aperture in thermal shield when the spacecraft is near the Sun. The strict thermal conditions of the environment have required optimizations which have changed old scheme with a new on-axis Gregorian telescope with external inverted occulter. With this new design, the thermal load on instrument components is reduced about 94% and the aperture in thermal shield is also reduced; furthermore, the on-axis configuration yields better optical performances.

1 The sounding rocket is an instrument-carrying rocket designed to take measurements and perform scientific experiments during its sub-orbital flight, usually from 50 to 1500 kilometers above the surface of the Earth. It is commonly use these rockets for testing new instruments before a space mission.

2.1 CORONAGRAPH OPTICAL LAYOUT

The new optical layout adopted for METIS is named *inverted coronagraph* and it is shown in Figure 5.

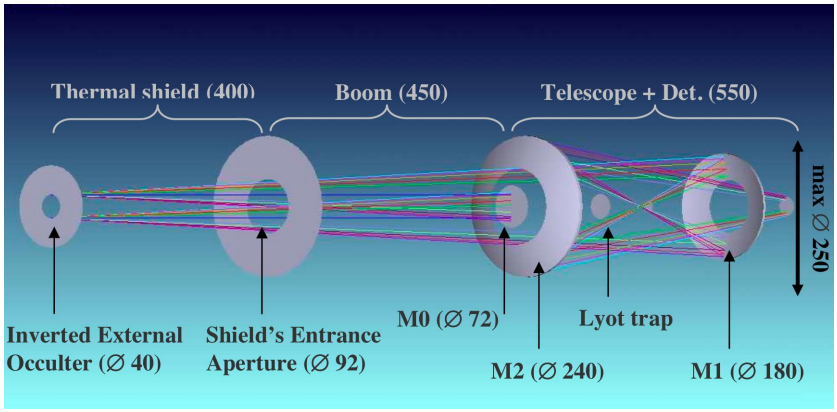

Figure 5: Optical layout of the inverted coronagraph adopted in METIS

Inverted coronagraph concept

The inverted external occulter (IEO) is a hole of 40 millimeters in diameter in the thermal shield of the spacecraft and it is the aperture of the instrument. Behind, a convex spheric mirror M0 is used for rejecting back through shield aperture the disk-light while the corona-light enters in the on-axis Gregorian telescope. The primary ellipsoidal mirror M1 collects the corona-light and constructs the image in the focal plane of the secondary ellipsoidal mirror M2 which focuses the corona image in a second focal plane behind the primary.

The sun-disk light diffracted from M0 is a potential source of noise inside the instrument as well as the corona-light diffracted from the inverted external occulter; an internal occulter and a lyot trap are used for suppressing the diffracted light from IEO and M0 respectively.

In the spacecraft is planned a door mechanism which close instrument aperture when METIS is not used. Instead, during time activity the spacecraft could be off-axis with the Sun center and the harmful disk-light can enter inside instrument; in order to avoid this problem, a mechanism for moving mirror M0 can be planned. Obviously, the mechanism should not degrade excessively the optical performances of the instrument for maximizing the scientific results during the spacecraft off-pointing. A first solution consists of moving the mirror M0 in a circumference centered in the center of the IEO but in this way the system is efficient only a offset along a single direction. An alternative could be a mechanism which translates M0 along the instrument

axial direction but the system loses efficiency in disk rejection and reduces the field of view. Finally, another solution could be a safe system which closes the instrument aperture when the illumination condition becomes dangerous for the instrument. Also a mechanism for adjusting the position of the internal occulter for compensating external inverted occulter misalignments and off-pointing spacecraft is required.

2.2 CORONAGRAPH OPERATION MODES

The coronagraph observes three wavelength using same telescope and this configuration allows two operation mode. In "UV mode" a narrow-band Al/MgF_2 filter selects a band of about 10nm in width centered at 121.6nm line. This filter works with an incident angle of 45° and it also reflects the visible wavelengths into a polarimeter as shown in Figure 6; in this operation mode, the EUV wavelength is not observed. The visible light

UV and visible path

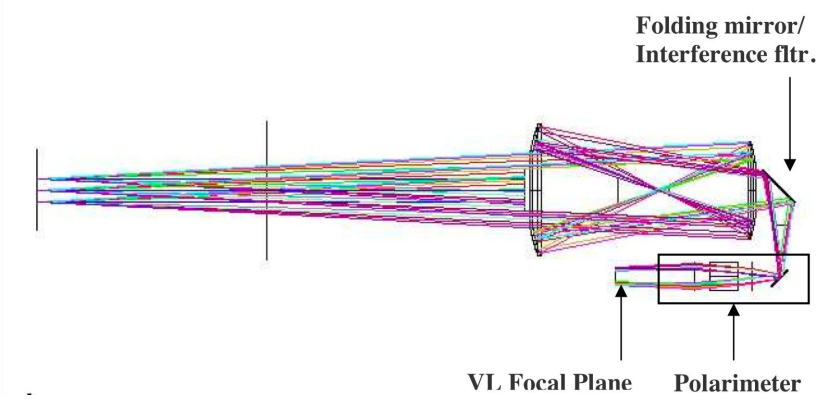

Figure 6: Visible light optical path inside METIS

polarimeter is composed by a liquid crystal variable retarder together with a fixed half-wave retarder and a liner polarizer in "*Sernamount*" configuration. The visible detector will be a CMOS Active Pixel Sensor which is more suitable to Solar Orbiter environment than a CCD.

When we want observe the HeII Lyman-α line, a mechanism exchanges the Al/MgF_2 filter with a double low pass Aluminum filter which rejects the longer wavelengths. In this condition, only 30.4nm line is imaged from the instrument and the operation mode is named "EUV mode". In both operation modes, the optical path of UV and EUV wavelengths is the same and it is shown in Figure 7. The UV and EUV detector is the same and it will be a photon counting with a 2kx2k format. The good op-

EUV path

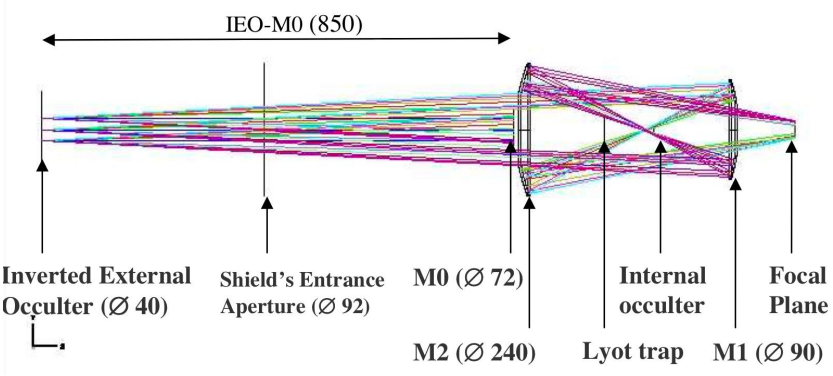

Figure 7: EUV and UV optical path inside METIS

eration of the instrument requires that the primary mirror M1 and the secondary mirror M2 reflect the 30.4nm line, 121.6nm line and the wavelengths in the range 500-650nm. As it is shown in the following chapters, this task is achieved by a multilayer coatings with an appropriate capping-layer.

2.3 SPECTROSCOPIC CHANNEL INSIDE METIS

Spectroscopic channel description

The coronagraph layout allows to realizing also an EUV/UV spectroscopic channel without substantial changes in the structure. A sector of the primary mirror M1 is used for feeding a multi-slit spectrometer obtained replacing a sector of secondary mirror M2 with a grating; the spectrum diffracted is imaged from a sector of the UV/EUV detector that is not used in coronal imaging. The spectroscopic path is shown in Figure 8.

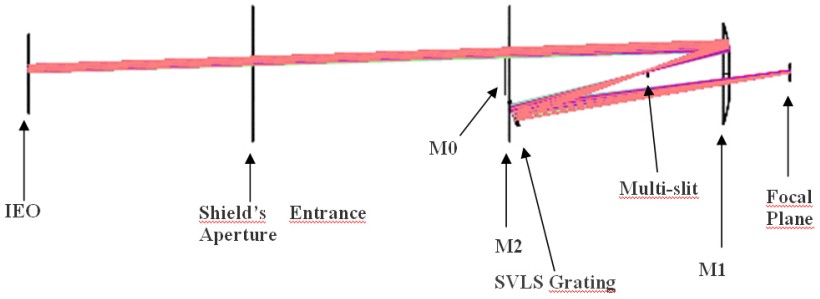

Figure 8: Spectroscopic path inside METIS

The grating is a spherical varied line-spaced with 1800 lines/mm which diffracts the 121.6nm line at first order and the 30.4nm line at fourth order on the same location in focal plane. The gratings works with incidence angle α of $4,15^{o}$ and the diffraction angle

β at fourth order of 30.4nm line is $8,42^o$ as we can compute by the classical grating equation. We note that also this optical component requires a multilayer coating for reflecting the EUV and UV wavelengths.

The multi-slit input section selects the angular field of view from the Sun's center: in current design, can be selected $1,4^o$ or $1,7^o$ or 2^o of field of view and the sector reserved to spectroscopy is about 32^o out of the total 360^o at minimum perihelion (see Figure 9).

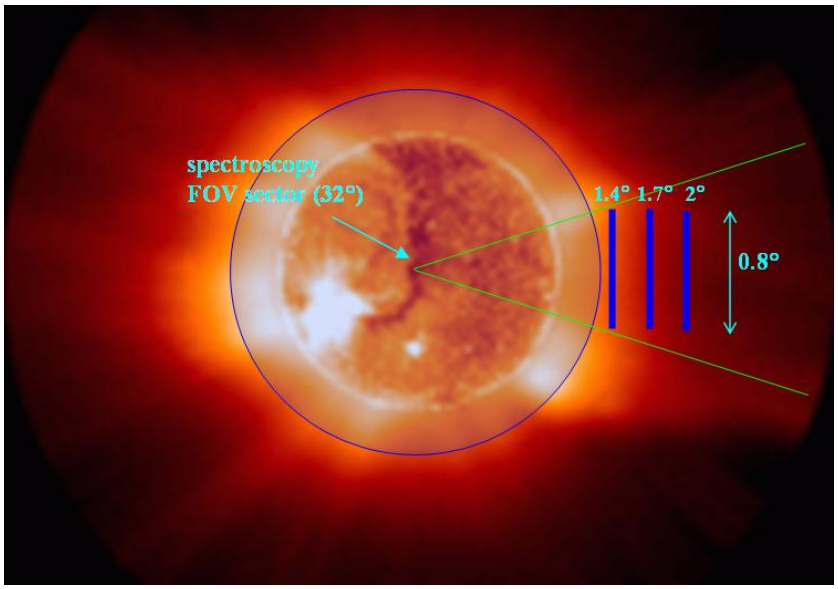

Figure 9: Field of view at $0,23$AU for the spectroscopy

2.4 THERMAL ANALYSIS

During the mission, METIS will observe the Sun through an opening in the thermal shield and the spherical rejection mirror M0 will be exposed to the direct solar flux while the remaining coronal light flux could increase the temperature inside the telescope.

At the perihelion, the solar flux is approximately $25000W/m^2$ and a thermal analysis can be performed for driving the mechanical design of METIS. The general specifications provided by [8] suggest that the temperature of the optical components inside the telescope should never exceed the 50°C: the current mechanical design is shown in Figure 10. The thermal model has shown that the critical components is the reject mirror M0 because internal temperature distribution is strongly driven by

Thermal analysis of METIS

the temperature of its rear face. With an accurate design of this mirror, the thermal simulations have shown that the temperature reached from primary and secondary mirror is about 60°C.

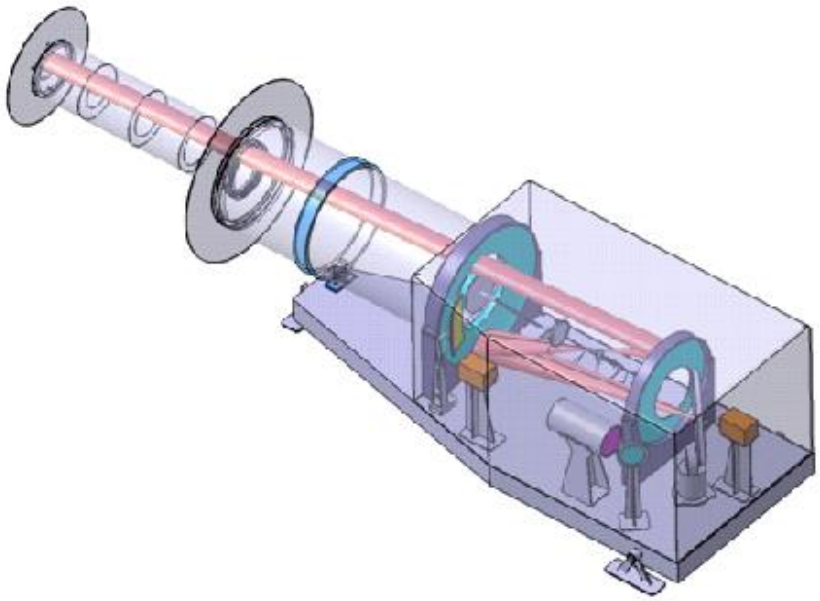

Figure 10: Mechanical design of METIS

3 INTRODUCTION TO MULTILAYER COATINGS THEORY

During last decades, the EUV and x-ray range is become important in many research field and apposite instruments operating at these wavelengths have been designed. This range is required in solar physics because at these wavelengths we can observe the plasma emissions corresponding to Fe-IX (at 17.1nm), Fe-XII (at 19.5nm), Fe-XV (at 28.4nm), He-II (at 30.4nm) and Fe-XVI (at 33.5nm) useful to understand the physics of the solar activities (Figure 11).

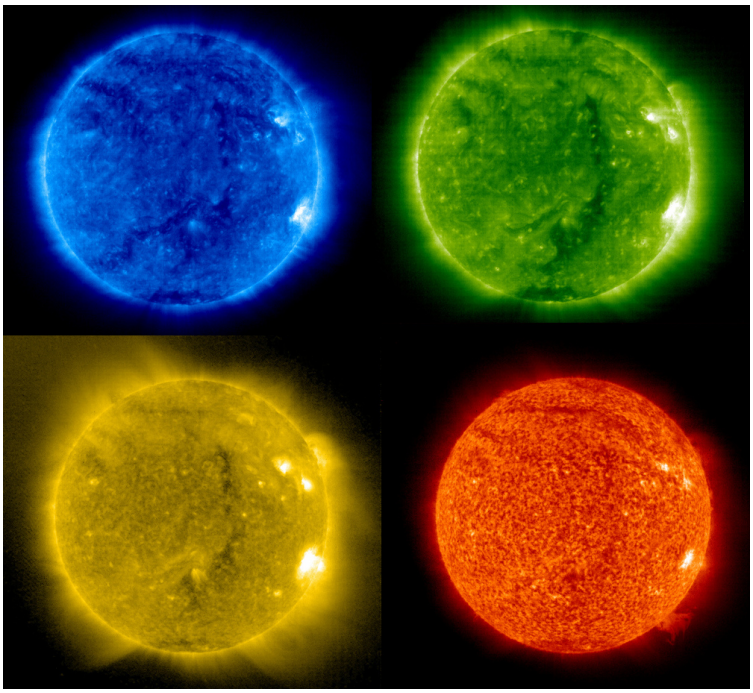

Figure 11: An image of the Sun in false colors at 17.1nm (blue), 19.5nm (green), 28.4nm (yellow) and 30.4nm (red).

The main problem for the instruments working in EUV and Soft-x ray range is the efficiency of the optical components because the reflectivity of materials at normal incidence is close to zero in these wavelengths. An acceptable solution uses grazing configuration systems but these optical layouts cannot be used in imaging applications and the develop of an high efficiency

normal incidence optics is required: the best results have been obtained using the multilayer optical coatings. Example of successful missions in which the multilayer coating are used are SOHO [4, 11] and TRACE [25]. Also METIS, for reflecting the line 30.4nm, will require optical multilayer coatings.

3.1 OPTICAL CONSTANTS IN EUV SPECTRAL RANGE

The propagation of electromagnetic waves is described from the Maxwell's equations. In the light propagation theory it is convenient to study a particular family of waves named "plane waves" because they are a mathematical base of the solutions of the Maxwell's equations.

Plane waves

Solving the equations, an elctromagnetic plane wave propagating in the x-direction in a material without losses is described by [1]

$$E(t,x) = E_0 e^{-j(Kx-\omega_0 t)} \tag{3.1}$$

were E_0 is the field amplitude at x=0, ω_0 is the angular frequency and K is the wave vector. We have also

$$K = \frac{2\pi}{\lambda_0} n \tag{3.2}$$

where n is the real refractive index of the material and λ_0 is the wavelength in vacuum.

When we work in the visible light range, the free losses material is an hypothesis occurred in almost all cases but when the wavelength decrease, the materials become absorbing and the wave vector K becomes complex. For holding the formalism developed in the case of free losses material, we can define the complex refractive index

Complex refractive index

$$\mathbf{n_c} = n + j\beta \tag{3.3}$$

where n and β are the material optical constants. β is named extinction coefficient and establish the wave absorption while n is name still refractive index.

After to have defined the optical constants, we can now describe an electromagnetic wave with wavelength in the soft X-ray using equation (3.3) in (3.2). We have

$$E(t,x) = E_0 e^{-j(\frac{2\pi}{\lambda_0}\mathbf{n_c}x-\omega_0 t)} = E_0 e^{-\frac{2\pi}{\lambda_0}\beta x} e^{-j(\frac{2\pi}{\lambda_0}nx-\omega_0 t)} \tag{3.4}$$

1 Solution is expressed in the symbolic Steinmetz's transform domain where we can describe the amplitude, phase and propagation proprieties of a plane wave by a complex number.

As we can see, in the equation (3.4) the term $e^{-\frac{2\pi}{\lambda_0}\beta x}$ takes into account the material absorption while the term $e^{-j(\frac{2\pi}{\lambda_0}nx-\omega_0 t)}$ describe the wave propagation in the medium. Remembering that the intensity of a wave is proportional to the square module of the electric field, from (3.4) we also define the linear absorption coefficient

Absorption coefficient

$$\alpha = \frac{4\pi}{\lambda_0}\beta \tag{3.5}$$

that describes the attenuation of the intensity of the wave propagating through thickness d of material by

$$I = I_0 e^{-\alpha d}$$

Complex refractive index in EUV range

In the EUV, for energies between $30eV$ and $30keV$, the optical constants, and consequentially the complex refractive index, can be computed directly from the atomic scattering factors. In particular, for a compounded material with a own composition and density, the optical constants are related to the atomic scattering factor f_1 and f_2 by

$$\mathbf{n_c} = 1 - \delta + j\beta = 1 - N_a \rho \frac{\lambda^2 e^2}{2\pi m_e c^2} \frac{\sum_i x_i (f_{1,i} - j f_{2,i})}{\sum_i x_i A_i} \tag{3.6}$$

where the sums range over each of the chemical elements that comprise the compound, the x_i are the relative concentrations of each elements and A_i is the associated atomic densities; in (3.6) are also used the elementary electron charge e, the electron mass m_e, the light speed in vacuum c and the Avogrado's number N_a. The approximation (3.6) is computed with the hypothesis that in this region the energy is enough high to consider negligible the interaction with the valence electron but, at longer wavelength, this interaction became significant and the approximation is no longer valid. The atomic scattering factors can be retrieved through experimental measures in the cross section of the elementary matter and nowadays many database are available with the atomic scattering factors.

We can also define the dielectric function $\epsilon(\lambda)$ as

$$\mathbf{n_c} = \sqrt{\epsilon(\lambda)}$$

This function record all the effects of the materials aggregate nature like chemical bound and the collective excitations.

3.2 THE MULTILAYER COATINGS

A multilayer coating is constituted by an alternating sequence of thin films, one with hight absorption (named absorber) and

one less absorbent (named spacer) as shown in Figure 12 and Figure 13.

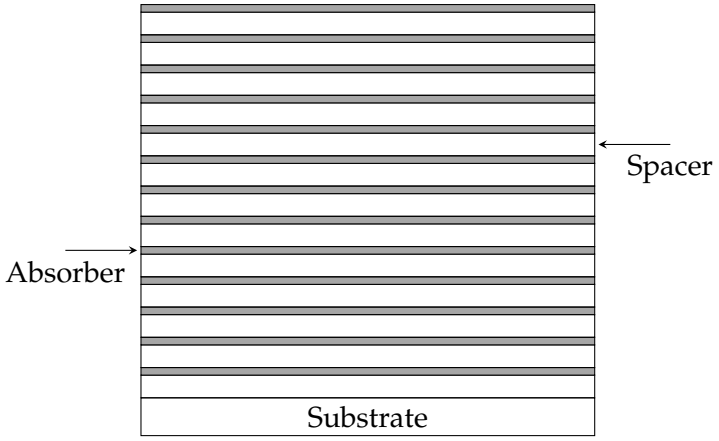

Figure 12: Structure of a periodic multilayer coating

The choice of materials couples are led from many factors. A method consist to choose two materials which have hight optical contrast (different optical constants). In the soft-x ray and x-ray the spacer materials consists of a low Z (where Z is the atomic number) material and often they are chosen to have an absorption edge just above the desired wavelength for obtaining a small β and a δ negative. The absorber materials instead are a high Z material and they are chosen to have as large as possible difference in δ from the spacer and, if it is possible, small β.
Obviously, we can make a good multilayer coating choosing two materials which have low optical contrast and low absorption; in this condition the electromagnetic wave interacts with many interfaces respect to previous cases and the high reflectivity is achieved by these many contributions.

In this stack the hight reflectivity, also in normal incidence, is derived from the interference of the Fresnel components reflected in the interfaces between the two materials.

Multilayer description parameters

Let d_{spacer} be the thickness of the spacer material and $d_{absorber}$ the thickness of the absorber material in a multilayer stack. We define the multilayer period p as

$$p = d_{spacer} + d_{absorber} \tag{3.7}$$

and the multilayer ratio γ as

$$\gamma = \frac{d_{spacer}}{p} \tag{3.8}$$

These parameters, with the number N of the spacing layers (or absorber layers), describe uniquely the structure of a periodic

multilayer coating. We can also obtain an aperiodic structure where the thickness of each layer has been optimized for matching the relative phase of the various Fresnel components reflected and inter-reflected by multiple paths into stack, so that in the outgoing waves the various components can interfere constructively or destructively. In these aperiodic multilayer coatings the parameters defined in (3.7) and (3.8) lose significance and the optical structure must be described listing each layer.

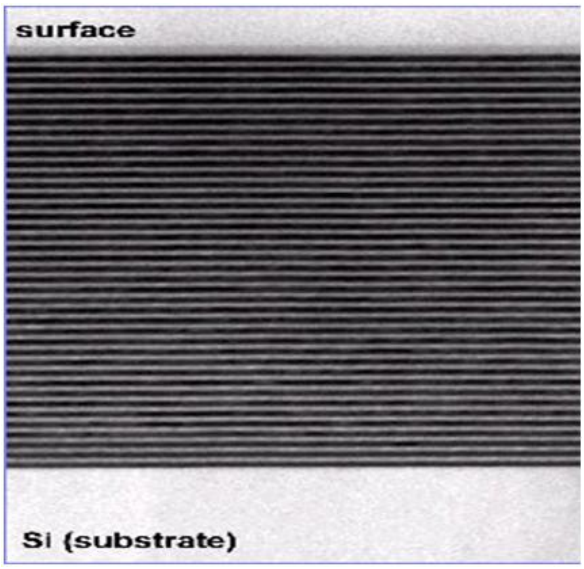

Figure 13: An image of a multilayer coating obtained by Transmission Electron Microscopy (TEM)

3.3 REFLECTION AND TRANSMISSION AT AN INTERFACE

Computations of the optical functions of the multilayer films can be based on application of the Fresnel equation which describe the reflection and transmission of an electromagnetic plane wave incident at an interface between two dissimilar materials characterized respectively from an own complex refractive index. Let S_{ij} be the ideal interface between semi-infinite layer $i-th$ and semi-infinite layer $j-th$. The complex refractive index of each layer is respectively $\mathbf{n_i}$ and $\mathbf{n_j}$. The incident wave vector makes an angle θ_i respect to the interface normal and $\mathbf{E_i}$ is the complex electric field amplitude as expressed in (3.4). The situation described above is reported in Figure 14. Solving the

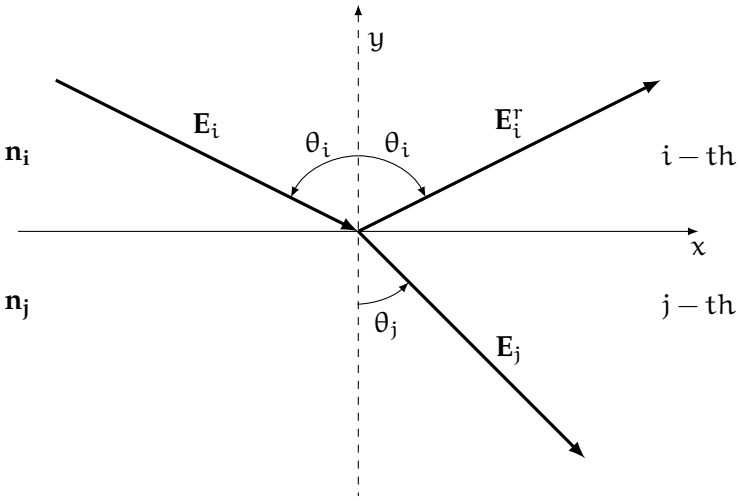

Figure 14: Representation of a plane wave incident into an ideal interface between two optically dissimilar materials

Fresnel's equations

Maxwell's equations with these assumptions, the amplitude of the reflected $\mathbf{E_i^r}$ and transmitted $\mathbf{E_j}$ electric field are given by

$$r_{ij}^s = \frac{\mathbf{E_i^r}}{\mathbf{E_i}} = \frac{\mathbf{n_i}\cos\theta_i - \mathbf{n_j}\cos\theta_j}{\mathbf{n_i}\cos\theta_i + \mathbf{n_j}\cos\theta_j} \tag{3.9}$$

and

$$t_{ij}^s = \frac{\mathbf{E_j}}{\mathbf{E_i}} = \frac{2\mathbf{n_i}\cos\theta_i}{\mathbf{n_i}\cos\theta_i + \mathbf{n_j}\cos\theta_j} \tag{3.10}$$

for s polarization (that has the electric field perpendicular to the plane of incidence) and

$$r_{ij}^p = \frac{\mathbf{E_i^r}}{\mathbf{E_i}} = \frac{\mathbf{n_i}\cos\theta_j - \mathbf{n_j}\cos\theta_i}{\mathbf{n_i}\cos\theta_j + \mathbf{n_j}\cos\theta_i} \tag{3.11}$$

and

$$t_{ij}^p = \frac{\mathbf{E_j}}{\mathbf{E_i}} = \frac{2\mathbf{n_i}\cos\theta_i}{\mathbf{n_i}\cos\theta_j + \mathbf{n_j}\cos\theta_i} \tag{3.12}$$

for p polarization (that has the electric field parallel to the plane of incidence). The relation between θ_i and θ_j is still determined from Snell's law [2]

The Snell's law

$$\mathbf{n_i}\sin\theta_i = \mathbf{n_j}\sin\theta_j \tag{3.13}$$

2 When $\mathbf{n_i}$ is a complex number also θ_i is complex and its physical meaning is lost; new refracted angle can be computed determining the new constant phase planes [21, chap. 13].

Unfortunately, when we product a multilayer coatings, the interface between two materials are not abrupt but we will have roughness and diffuseness that change the refraction index across the interface and then optical performances of the coating. In order to account no-ideal interface effects, we can follow the formalism developed by [32] and we define the normalized average dielectric function $p(y)$ as

No-ideal interface

$$p(y) = \frac{\iint \epsilon(x,z)\,dx\,dz}{(\epsilon_i - \epsilon_j)\iint dx\,dz}$$

where, for $\epsilon(x,z)$, we have also

$$\lim_{y\to+\infty} \epsilon(x,z) = \epsilon_i$$
$$\lim_{y\to-\infty} \epsilon(x,z) = \epsilon_j$$

It can be shown that non-abrupt interfaces effects can be approximated by multiplying the Fresnel's reflection coefficient by the function $\tilde{w}(s)$ defined as the Fourier transform of [32]

$$w(y) = \frac{dp}{dy}$$

The new corrected Fresnel reflection coefficients are given by

$$r'_{ij} = r_{ij}\tilde{w}(s_i)$$

with

$$s_i = \frac{4\pi\cos\theta_i}{\lambda}$$

We want underline that the changing depend only on the average variation (over x and z) in index across the interface. Consequently, the effects in reflectivity performances are the same if the interface is rough (in which the transition between two materials are abrupt), if in the interface there are diffusions (in which the refractive index varies smoothly along the y direction) or if the interface is a combination of the two.

The width of each interface profile function is characterized by the parameter σ (see Figure 15) which is a measure of either an rms interfacial roughness, in the case of a purely rough interface, or interface width, in the case of a purely a diffuse interface, or some combination of the two properties in the case of an interface that is both rough and diffuse; it is the parameter σ (along with the choice of interface profile function) that is specified to account the effects of interface imperfections using the modified Fresnel coefficient approach. There are many useful

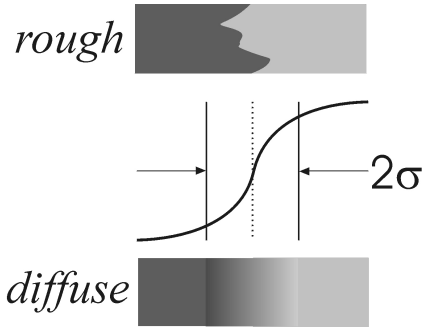

Figure 15: Profile function $p(y)$ for describing the rough or diffuse interface.

profile function $p(y)$ for describing the nonideal interface: usually, it is convenient assuming $p(y)$ as a Normal error function with standard deviation σ; the Fresnel transmission coefficients are then computed by

$$r'_{ij} = r_{ij} e^{-\frac{s_i^2 \sigma^2}{2}}$$

The intensity is proportional to squared modulus of the electric field amplitude and also the reflected or transmitted intensity is determined by the squared modulus of the Fresnel coefficients for each polarization. However, in the Solar physics observations the multilayer coatings must reflect the ordinary light which is unpolarized. In this case, we can obtain an approximation of the reflectivity considering average between the reflectivity in s and p polarizations. We have the intensity reflection coefficient (also named Reflectance) defined by

Reflectance and Transmittance

$$R = \frac{|r^s|^2}{2} + \frac{|r^p|^2}{2} = \frac{R_s}{2} + \frac{R_p}{2} \tag{3.14}$$

and, likewise, the intensity transmission coefficient (Transmittance) is

$$T = \frac{|t^s|^2}{2} + \frac{|t^p|^2}{2} = \frac{T_s}{2} + \frac{T_p}{2} \tag{3.15}$$

absorptance

We also underline that when the material is absorbent, we have $T + R < 1$ and we can define the absorptance A by

$$A = 1 - T - R$$

When a plane wave is in normal incidence, we can assume $\theta_i \simeq 0$ and in equations (3.9) and (3.11) the $\cos\theta_i \simeq 1$; from (3.14) we have

$$R = \frac{(\delta_i - \delta_j)^2 + (\beta_i - \beta_j)^2}{4}$$

in which we note that the reflectance at the materials interface is increased if the optical constants of materials are very different: this give us a condition for designing a high reflectivity single interface.

3.4 OPTICAL FUNCTIONS OF MULTILAYER STACK

The reflectivity can be increase by multilayer. In this structure, the portion of wave reflected in a interface interfering constructively with the portion of wave reflected in the interface above as shown in Figure 16.

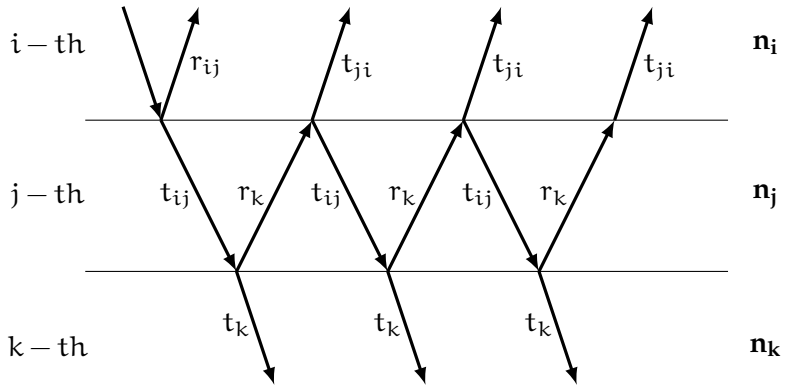

Figure 16: Schematic propagation of a plane wave in a generic layer of a multilayer stack

When the plane wave propagates in the layer $j-th$, it accumulates a phase delay which determines if the interference is constructive or destructive. With reference to Figure 17, the optical path of the wave reflected from interface S_{ij} is given by

$$OP_i = \mathbf{n_i}\overline{AD} = \mathbf{n_i}\overline{AC}\sin\theta_i = 2\mathbf{n_i}d_j\tan\theta_j\sin\theta_i$$

and using the Snell law (3.13) we can write

$$OP_i = 2\mathbf{n_j}\frac{\sin^2\theta_j}{\cos\theta_j}d_j$$

The optical path of the wave transmitted in the layer $j-th$ is given by

$$OP_j = \mathbf{n_j}\overline{ABC} = 2\mathbf{n_j}\frac{d_j}{\cos\theta_j}$$

Now, we can compute the difference between the optical path and we have

$$\Delta OP = OP_j - OP_i = 2\mathbf{n_j}d_j\cos\theta_j$$

Phase delay in a thin film

and, consequently, the phase delay is

$$\Phi = \frac{2\pi}{\lambda} 2\mathbf{n_j} d_j \cos\theta_j \tag{3.16}$$

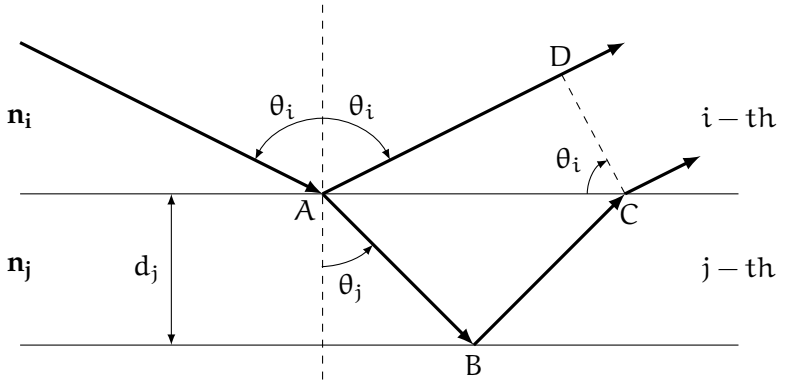

Figure 17: Schematic propagation in a thin layer for determining the phase delay

The total reflection of a wave in the interface S_{ij} is therefore the sum of the all reflection occurring in $j-th$ layer (which are theoretically infinite):

$$r_j = r_{ij} + t_{ij} t_{ji} r_k e^{j\Phi} \sum_{m=0}^{\infty} \left[r_{ji} r_k e^{j\Phi} \right]^m \tag{3.17}$$

where the imaginary term $e^{j\Phi}$ takes into account the phase delay in the layer $j-th$, r_{ij}, r_{ji}, t_{ij}, t_{ji} are the Fresnel coefficients which describe the reflection or transmission in a interface and r_k is the total equivalent reflection in the top of the layer $k-th$. In (3.17), we can solve the geometric series and we obtain

$$r_j = r_{ij} + \frac{t_{ij} t_{ji} r_k e^{j\Phi}}{1 - r_{ji} r_k e^{j\Phi}}$$

and, from Fresnel coefficients (3.9) and (3.10), we verify the relationship

$$t_{ij} t_{ji} + r_{ij}^2 = 1$$

Considering also that $r_{ij} = -r_{ji}$, we obtain the total equivalent reflection on the top of the layer $j-th$

$$r_j = \frac{r_{ij} + r_k e^{j\Phi}}{1 + r_{ij} r_k e^{j\Phi}} \tag{3.18}$$

With similar reasoning, for transmission we have

$$t_j = \frac{t_{ij} t_k e^{j\Phi}}{1 + r_{ij} r_k e^{j\Phi}} \tag{3.19}$$

Total reflection and transmission of a multilayer coating

Now, for computing the total reflection or transmission of the stack, we must apply the equations (3.18) and (3.19) recursively, starting at the bottom-most layer: obviously, these calculations must be performed separately for s polarization and p polarization using appropriate Fresnel's coefficients.

Once computed the total reflection coefficients r^s and r^p we can obtain the reflectance at ordinary light by

$$R = \frac{|r^s|^2}{2} + \frac{|r^p|^2}{2} = \frac{R_s}{2} + \frac{R_p}{2}$$

and the transmittance by

$$T = \Re \left[\frac{\mathbf{n_s} \cos\theta_s}{\mathbf{n_a} \cos\theta_a} \right] \cdot \left[\frac{|t^s|^2}{2} + \frac{|t^p|^2}{2} \right] = \frac{T_s}{2} + \frac{T_p}{2}$$

where $\mathbf{n_s}$ and $\mathbf{n_a}$ are the complex refractive index of substrate an ambient respectively.
Finally, the phase delays of the reflected and transmitted waves are given by

$$\phi_r = \arctan \frac{\Im[r]}{\Re[r]}$$
$$\phi_t = \arctan \frac{\Im[t]}{\Re[t]}$$

When the plane wave interacts with multilayer structure, in each layer we observe an superposition between positive-going (generated from transmission in the interface above) and negative-going (generated from reflection in the interface below) fields: this phenomenon generate a standing wave which must be studied for computing the electric field intensity as a function of depth in multilayer stack. Let us consider the $i-th$ layer and the interface between it and $j-th$ layer where we have both positive-going and negative-going plane waves. Solving Maxwell's equations in this case, we can show that the positive-going and negative-going field amplitudes at a distance y above the interface are given by

Electric field amplitude in a multilayer coating

$$\mathbf{E}_i^+(y) = \frac{1}{t_{ij}} e^{-j\Phi_i(y)} \mathbf{E}_j^+(0) + \frac{r_{ij}}{t_{ij}} e^{-j\Phi_i(y)} \mathbf{E}_j^-(0) \tag{3.20}$$

and

$$\mathbf{E}_i^-(y) = \frac{r_{ij}}{t_{ij}} e^{j\Phi_i(y)} \mathbf{E}_j^+(0) + \frac{1}{t_{ij}} e^{j\Phi_i(y)} \mathbf{E}_j^-(0) \tag{3.21}$$

where

$$\Phi_i(y) = \frac{2\pi}{\lambda} \mathbf{n_i} y \cos\theta_i$$

and we have indicated with $\mathbf{E}_j^+(0)$ and $\mathbf{E}_j^-(0)$ the field amplitudes at the top of the $j-th$ layer. Again, a recursive approach can be used to compute the field amplitudes throughout the stack, starting at the bottom-most layer with the field amplitudes in the substrate given as $\mathbf{E}_s^+(0)$ and $\mathbf{E}_s^-(0)$. We can also express the net reflection and transmission coefficients of the film as function of the field amplitudes in the ambient by

$$r = \frac{\mathbf{E}_a^-(0)}{\mathbf{E}_a^+(0)}$$

and

$$t = \frac{1}{\mathbf{E}_a^+(0)}$$

The total electric field amplitude at y position can be computed by sum of the two components $\mathbf{E}^+(y)$ and $\mathbf{E}^-(y)$ obtaining also

$$I(y) = \left|\mathbf{E}^+(y) + \mathbf{E}^-(y)\right|^2$$

Obviously, previous analysis must be performed for s and p polarizations.

Let us now consider a multilayer structure made of two film materials of complex index $\mathbf{n_i}$ and $\mathbf{n_j}$, thickness d_i and d_j, and period $p = d_i + d_j$. The reflectivity will add up to a large value when all periods add in phase. The phase delay in equations (3.18) or (3.19) should be $2m\pi$ where m express the reflectivity at $m-th$ order. Considering as ambient the vacuum ($n_0 = 1$), defining the grazing angle $\varphi_i = \frac{\pi}{2} - \theta_i$ and considering $\beta_i \ll \delta_i \ll 1$ from equation (3.16) we obtain

The Bragg's law

$$m\lambda = 2p \sin\varphi_0 \sqrt{1 - \frac{2\delta}{\sin^2\varphi_0}} \tag{3.22}$$

where

$$\delta = \frac{d_i\delta_i + d_j\delta_j}{d_i + d_j}$$

is the weighted average index of two materials in the coating and with φ_0 we have indicated the grazing angle in the top of the multilayer coating.
The expression (3.22) is named "Bragg's condition" and it appears often in the literature without square root because, for deriving it in the x-ray range, the $\delta = \beta = 0$ condition are assumed. This relation gives the relationship between period, wavelength and incidence angle and it is usually used for determining the period p of a multilayer structure tuned at a specific λ.

3.5 MULTILAYER COATINGS BANDWIDTH

Another significant parameter in a multilayer coating is the bandwidth especially when we want select a specific line very close to others noise line; the bandwidth is defined by the criteria "full width at half maximum" (FWHM).

Estimation of the bandwidth is a problem very complex but an approximation can be obtained by observing that multilayers provides a temporally coherent responce: for increasing the reflectivity, the wave reflected from the lowest layer in the stack must add coherently with the wave reflected in the top layer. This physical limit means that the total thickness of the multilayer is proportional to the coherence length of the multilayer and we have

$$p \cdot N \simeq L_{coh} = \frac{\lambda^2}{\Delta\lambda} \tag{3.23}$$

where p is the multilayer period, N is the number of periods and L_{coh} is the coherent length; from (3.23) we also obtain

$$\Delta\lambda \propto \frac{1}{N}$$

if we suppose the total penetration of the multilayer coating. Unfortunately, the materials have the extinction coefficient β and, consequentially, the absorption coefficient α defined by (3.5) which determines the maximum penetration length. Now, from Bragg's condition (3.22) we can estimate the period p for tuning the multilayers at a desired wavelength λ and from (3.5) the equivalent penetration length l_{pen}. Finally, we can compute the number of penetrated periods; we have

$$N_{max} \simeq \frac{l_{pen}}{p} = \frac{\sin^2\varphi}{2\pi\beta}$$

where φ is the grazing angle of the plane wave in top of stack.

From this approximate analysis, we have find that $\Delta\lambda \propto N^{-1}$ if $N < N_{max}$ but $\Delta\lambda \propto N_{max}^{-1}$ if $N > N_{max}$.

4 DESIGN OF OPTICAL MULTILAYER COATINGS FOR METIS

Multilayers based on periodic Mo/a-Si structure have been used in many space experiments (for example [4], [14],[16]) and they have always provided good long-term and thermal stability [28] which is essential in a space mission such as Solar Orbiter. Unfortunately, around 30.4nm line, the reflectivity of these multilayers is usually less than 30%. Multilayers Mg/SiC, used in SCORE instrument on board of a sounding rocket, provide much higher reflectivity at 30.4 nm and with a specific capping layer the reflectivity at 121.6 nm and in the visible spectral range can be also controlled (see Figure 18) [30]. Unfortunately, these

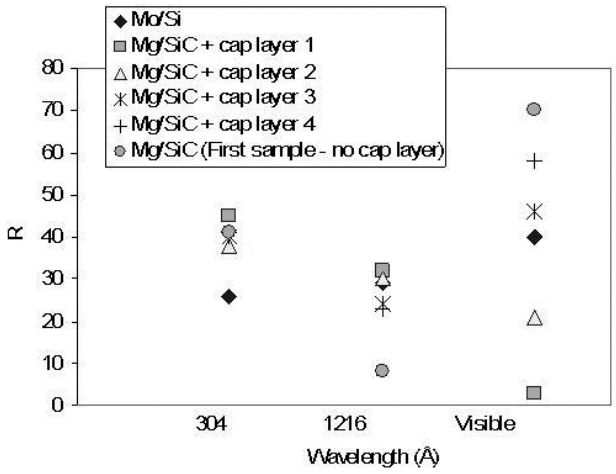

Figure 18: Comparison between multilayer SiC/Mg with different capping-layers.

coatings have not proved being stable over the time and therefore we are very skeptical with respect to their usage in a long space mission. Others materials couples could be used to improve the reflectivity [17, 37], but there are not detailed studies which investigate their stability in space applications.

New multilayer coatings proposed for METIS

Now, we want propose new designs based on a Mo/a-Si multilayers (very standard couple) overcoated by four different capping-layers; we have designed a Ruthenium capping-layer [22, 23, 26, 27] which is already partially tested in critical environments be-

cause used in EUV photolithography application, two Iridium capping-layers and a Tungsten capping-layer which are stable over the time and they do not oxidize. Finally, an innovative design based on Si/Ir and Al/Zr (Aluminum/Zirconium) materials couple has been also analyzed.

4.1 DESIGN METHOD

In the design procedure, the capping layer solution is adopted for improving the reflectivity and together obtaining a protective layer. In particular, with the periodic structure we tune the reflectivity peak at the desirable EUV wavelength and then, we design a capping-layer structure, usually with different materials, for improving reflectivity in UV and visible spectral range without compromise the performance in EUV wavelength; obviously, for a advantageous result, the capping-layer materials must be stable in space environment and chemically compatible[1] with the materials which composing the periodic multilayer structure.

Standing wave design method

Correct optimization should consider the standing wave formed by the superposition of incident and reflected waves in the multilayer structure. Hight reflectivity at a precise incidence angle requires that the nodes of the standing wave are localized around the position of the absorber material and consequently the thicknesses of the periodic structure can be optimized [31, chap. 8]. Since the materials chosen in our capping-layer are absorbent in EUV range, the uppermost layers must be dimensioned in order to position a standing wave node in the topmost layer [20]. This optimization method is useful also we want improve spectral filtering [33, chap. 3] but in our case is not necessary because METIS analyzes the He-II line which is more brighter then Fe-XV and Fe-XVI near-lines.

Summarizing, the optimization step are

1. design of the periodic multilayer structure in order to have maximum reflectivity peak at desirable EUV wavelength.
2. choice of capping-layer material which is chemically compatible with the topmost layer of the multilayer.
3. optimization of the uppermost layers in order to preserve or improve reflectivity at EUV range and increase the re-

1 In this context, chemically compatible means also that the capping-layer material does not reacts chemically with the material in top of the multilayer structure.

flectivity at UV and visible range; in fact, the uppermost layers are optimized in order to positioning the standing wave node in the topmost layer.

4.2 SIMULATIONS RESULTS

The design performances have been evaluated with IMD program [19] adopting default optical constants (cxro constants)[5]; when these constants are unavailable, the simulations have been performed with Palik's optical constants [3]. The incident angle considered in simulations is 5.00 degrees and the roughness interface is 0.5nm as suggested by David Windt.

4.2.1 Standard periodic Mo/Si multilayer

As first step, a Mo/Si multilayer (named ML0) working at 30.4nm has been designed (Table 3) and afterward we have designed some capping-layers for improving its performances.

Multilayer a-Si/Mo	
Period [p]	16,40 nm
Ratio [γ]	0,82
Period number [N]	35

Table 3: Periodic Mo/Si coatings optimized for 30.4nm line

It is useful consider, as reference, the optical performances of this multilayer without capping-layers. However, the oxidation effects must be considered and for optimizing the structure, we have added in topmost other 2nm of Silicon, about half of which will oxidize.

Capping-layer	
Material	**Thickness**
a-SiO_2	1 nm
a-Silicon	1 nm

From simulations, reflectance is 26% at 30.4nm (Figure 19), 27% at 121.6nm and 35% at 600nm.

Reflectance of classic Mo/Si multilayer coating ML0

We also note that if a multilayer coating is covered by a capping layer which can oxidize, it can lose its performances at 121.6

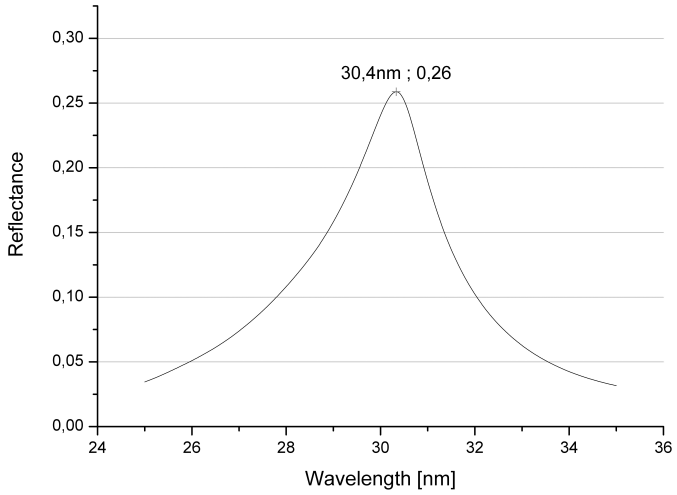

Figure 19: Reflectance of the Mo/Si base multilayer around 30.4nm line

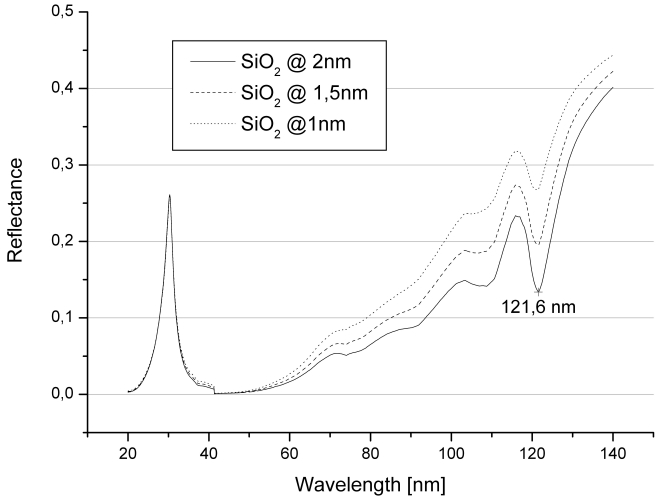

Figure 20: Effects of oxidation of the capping-layer in EUV range

nm as shown in Figure 20 for ML0 with native silicon oxide in top layer.

4.2.2 Iridium capping-layers for Mo/Si multilayer

The next cases are based on the Mo/Si multilayer ML0 over-coated with two different Iridium capping-layers (named CL1 and CL2); the structures are shown in Table 4. This material doesn't oxidize and therefore it is potentially good to reflect the 121.6nm line.

Capping Layer CL1	
Material	**Thickness**
Iridium (Ir)	2 nm
Molybdenum	2, 20 nm

Capping Layer CL2	
Material	**Thickness**
Iridium (Ir)	2 nm
a-Silicon	15, 40 nm
Molybdenum	2, 95 nm

Table 4: Structure of the Iridium capping-layers CL1 and CL2

Reflectance of ML0 with CL1 and CL2

From simulations, the reflectance of CL1 is 31% at 30.4nm, 22% at 121.6nm and 45% at 600nm while, using CL2, the reflectance is increased to 26% at 121.6nm but it drops to 28% at 30.4nm and to 40% at 600nm. In Figure 21 we can find a comparison between new Iridium capping-layers and multilayer base ML0.

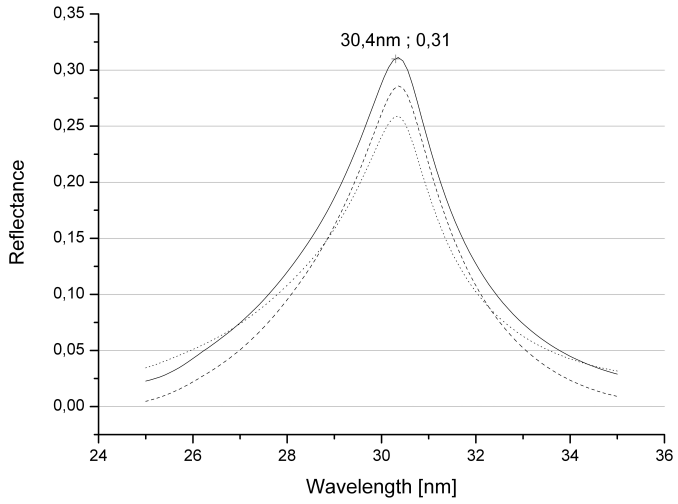

Figure 21: Reflectance comparison around 30.4nm between CL1 (continue curve), CL2 (dashed curve) and ML0 (dotted curve)

4.2.3 Ruthenium capping-layer for Mo/Si multilayer

In next case, a Ruthenium capping-layer (named CL3) is designed; the structure is reported in Table 5.

Capping-layer CL3	
Material	**Thickness**
Ruthenium (Ru)	2 nm
Molybdenum	2 nm
a-Silicon	14 nm
Molybdenum	3 nm

Table 5: Structure of Ruthenium capping-layer CL3

Reflectance of ML0 with CL3

From simulations, the reflectance is 31% at 30.4nm (see Figure 22), 33% at 121.6nm and 47% at 600nm.

The improvements of optical performances are considerable but the Ruthenium capping-layer could oxidize and we may lose its benefits. Unfortunately, the optical constants of this material are not available at 121.6nm line and we can not evaluate oxidation effects during design phase.

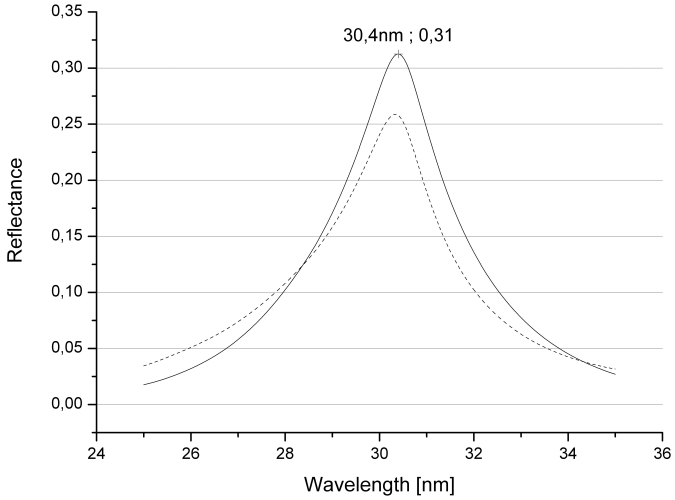

Figure 22: Comparison between multilayer base ML0 (dashed curve) and multilayer with Ruthenium capping-layer (continue curve).

4.2.4 Tungsten capping-layer for Mo/Si multilayer

In next case, we present the Tungsten capping-layer CL4 and its structure reported in Table 6. Tungsten, as Iridium, doesn't oxidize and therefore is useful for our purpose.

Capping-layer CL4	
Material	**Thickness**
Tungsten (W)	2nm

Table 6: Structure of Tungsten capping-layer CL4

Reflectance of ML0 with CL4

From simulations, the reflectance is 27% at 30.4nm (see Figure 23), 30% at 121.6nm and 39% at 600nm.

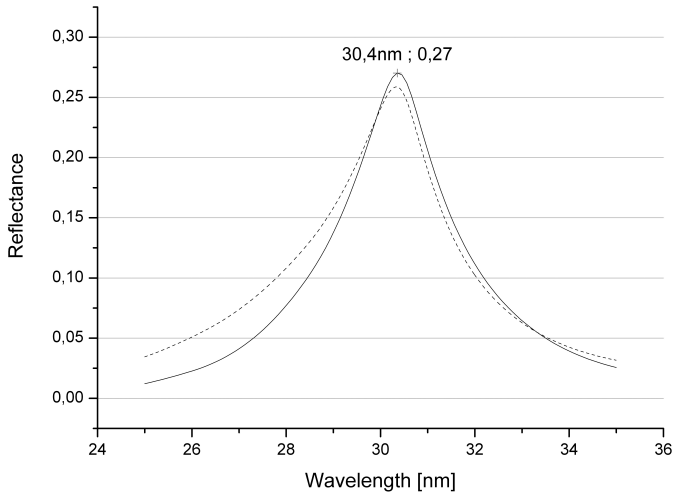

Figure 23: Comparison between multilayer base ML0 (dashed curve) and multilayer with Tungsten capping-layer (continue curve).

4.2.5 Design of new Ir/Si periodic multilayer

In next case, we present a new periodic multilayer based on Iridium and Silicon materials (named ML1). The coating is tuned at 30.4nm line and we have optimized the topmost layers for increase the optical performance. The structure obtained after design phase is reported in Table 7.

Capping-layer	
Material	**Thickness**
Iridium (Ir)	2,20 nm
a-Silicon	13,50 nm

Multilayer Ir/a-Si	
Period [p]	16,84 nm
Ratio [γ]	0,28
Period number [N]	30

Table 7: Structure of Ir/Si multilayer coating

Reflectance of Ir/Si multilayer coating

From simulations, the reflectance is 25% at 30.4nm, 24% at 121.6nm and 35% at 600nm.

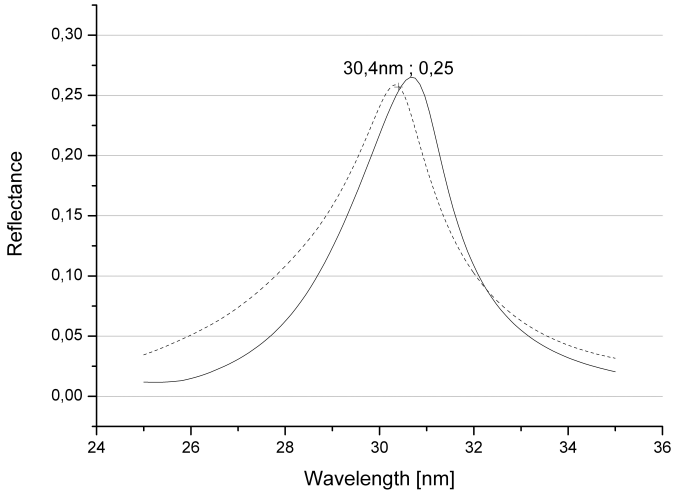

Figure 24: Comparison between multilayer Mo/Si ML0 (dashed curve) and multilayer Ir/Si ML1 (continue curve)

4.2.6 Design of new Zr/Al periodic multilayer

In next case, we present a new periodic multilayer based on Zirconium and Aluminum couple (named ML2). The coating is tuned at 30.4nm line and we have optimized an Aluminum capping-layer for increase the optical performance. The structure obtained after design phase is reported in Table 8.

Capping-layer	
Material	**Thickness**
Aluminum (Al)	4, 60 nm

Multilayer Zr/Al	
Period [p]	16, 20 nm
Ratio [γ]	0, 19
Period number [N]	30

Table 8: Structure of Zr/Al multilayer coating ML2 with Aluminum capping-layer

Reflectance of Zr/Al multilayer coating

From simulations, the reflectance is 27% at 30.4nm, 52% at 121.6nm. Unfortunately, the optical constants of the Zirconium

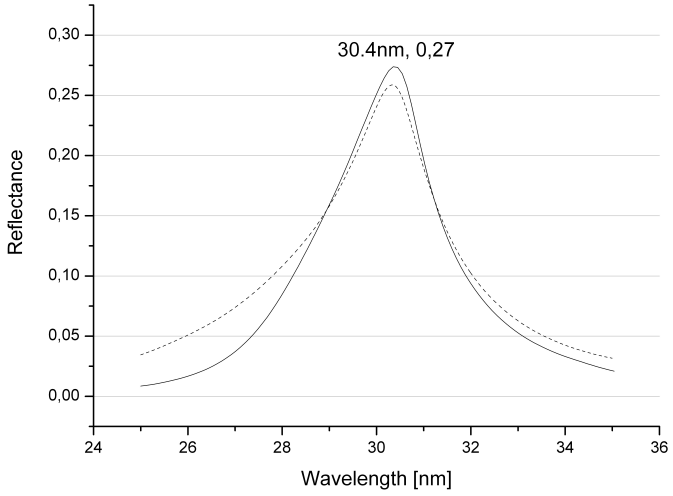

Figure 25: Comparison between multilayer Mo/Si ML0 (dashed curve) and multilayer Al/Zr ML2 (continue curve) around 30.4nm line

in the visible range are not available. However, we foresee high reflectance because in visible range it is determined predominantly from the interface between ambient and topmost Aluminum layer which is very reflective at these wavelengths.

Topmost thin protective layer for Zr/Al multilayer coatings

A problem of ML2 at 121.6nm could be instead given by oxidation of the topmost Aluminum layer. Another thin topmost layer can be added as protective layer without degrading excessively the reflectance; examples of materials can be SiC or B_4C and a optimized design is shown in Table 9.

SiC Capping-layer	
Material	**Thickness**
Silicon carbide (a-SiC)	2nm
Aluminum (Al)	16, 4nm

B_4C Capping-layer	
Material	**Thickness**
Boron carbide (B_4C)	2nm
Aluminum (Al)	3, 2nm

Table 9: Possible protective capping-layers for Zr/Al multilayer coating

From simulations, the new thin layer has reduced the reflectance but we have improved the stability. We have 26% at 30.4nm and 48% at 121.6nm if the protective layer is SiC or 25% at 30.4nm and 46% at 121.6nm if the protective layer is B_4C.

5 EARLY EXPERIMENTAL RESULTS AND TEST PLAN

The multilayer films designed in previous chapter were prepared from RXOLLC (New York, USA) by DC magnetron sputtering with a deposition system that has been described in [36]. Films were deposited onto polished Si(100) wafer segments measuring 16mm x 16mm. For each kind of multilayer coating, five samples were prepared during same depositing phase and we can consider identical their optical performances.

Unfortunately, the multilayer overcoated by Ruthenium capping-layer is not deposited yet and we can not evaluate its optical performances and the oxidation effects: this sample will be deposited soon and its test will be started.

In this chapter, we propose a test plan for investigating the stability in strict Solar Orbiter environment of these new samples and the discussion of the preliminary reflectance measurements. The samples measured are stored in standard condition for temperature and pressure (STP) and they will be considered as reference in all testing experiments. The experimental data are fitted for estimating the multilayer coatings parameters by IMD program [19].

5.1 MULTILAYER COATINGS TEST PLAN

During the mission Solar Orbiter, the multilayer must endure strict environments which are characteristic of the distances that the spacecraft will reach. A crucial point in the design phase is the tasting plain which allows us to evaluate the stability of the coatings when they are exposed in these environments. From the environmental analysis, the principal aspects which should be considered for our multilayer coatings are

- Natural aging of the coatings.
- Thermal stability of the coatings.
- Solar wind particles bombardments effects in the coatings.

Thermal stability of multilayer coatings

Generally, thermal stability is tested by thermal annealing:

multilayer is placed on a hotplate heated to the specified temperatures (much higher than working temperature) and it is usually held for one hour in order to promote any possible microstructural and chemical changes that might occur [15, 18, 24, 37]. With this method, we can identify the maximum temperature limit, we can understand how the multilayer degrades but we have not information about long-term heating effects. In fact, it may happen that a prolonged heating causes the same changes in a multilayer but at temperatures much lower than short-term thermal annealing. For investigate this aspect, in [24] the samples have been heated to the hottest working temperature expected during the mission and they have been held for long time: so, a valuation of long-term stability has been obtained. Furthermore, for space validation, these heating tests should be done in vacuum because we avoid any chemically reaction between materials in capping-layers and ambiance.

In METIS, thermal models have shown that the temperature reached during the mission from the telescope mirrors is around 60^{o}C: for testing the coatings for these mirrors, we can perform thermal cycles which heat the samples up to twice of the working temperature. The times of one orbit are very long and it is difficult reproduce a continuous annealing which simulates the real orbital conditions. However, the principal degradation occurs in the early hours of thermal annealing and so we can evaluate stability after few thermal cycles.

Aging of multilayer coatings

Even aging can lead modification of the optical properties but the evaluation of the phenomenon is very time expensive. In fact, if you want simulate the natural aging during a long mission, you must storage the samples for a period comparable with the duration of the mission [6]. This test is impossible because the available planning time for the mission is too short but we can perform a reduced aging of about one year.

Particles bombardments

In Solar Orbiter environment, the multilayers are also subject to continuous impacts with various types of particles. The effects in a multilayer's performances should be investigated for ensuring a good stability during the long-term space missions.

Unfortunately in scientific literature this issue has not been studied in detail. However, some experiments have been conducted and the results are very useful. In [29] the multilayer coatings have been bombarded with energetic protons and neutrons (energy around 30MeV) without finding any change in reflectivity while in [12] the bombings with protons at 100keV have been decreased the reflectance: this suggests a possible interaction between low energy protons and multilayers but the supposition must be thoroughly investigated in future.

Nothing we can say about impacts with heavy particles and even here a thorough investigation is required.

5.2 REFLECTANCE MEASUREMENTS AT 30,4NM LINE

The reflectance of multilayer coatings around 30.4nm line has been performed at BEAR (Bending magnet for Emission Absorption and Reflectivity) beamline in the synchrotron of Trieste (Italy) [34]. The reflectance has been evaluated in s-polarization and in p-polarization and then averaged to obtain the reflectance to unpolarized light.

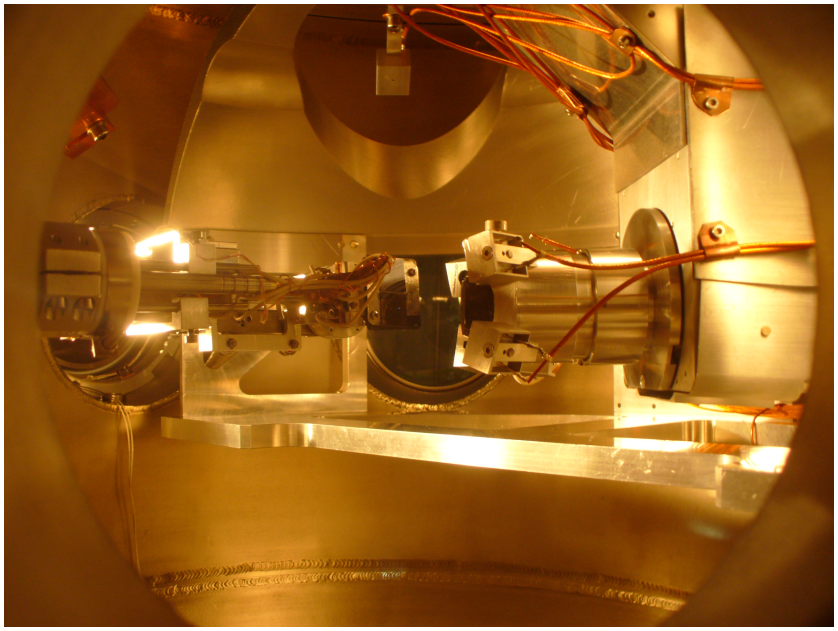

Figure 26: Our samples in BEAR chamber.

The accuracy and validity of Fresnel's coefficients approach used in the simulations, and of the structural parameters derived from the fits, depends crucially on the accuracy of the optical constants used in the calculation, on detailed knowledge of the layer and interface morphology, and on the condition of the surface especially in the EUV where thin surface contamination layers can strongly affect the normal-incidence reflectance. At the EUV wavelengths considered here, unfortunately, the availability of accurate optical constants remains poor, in general, in spite of continuing efforts to measure these quantities for technologically important materials. Also the chemical reactions which

could occur in the interface modify the reflectance performances and the model used in the simulations is not longer correct.

In our samples, a better fit of the experimental data is obtained using the optical constants of Tarrio [2] for Molybdenum as already shown in [37]. In all simulations we have used a 0,4nm interface roughness which seems reasonable as shown from Atomic Force Microscopy (AFM) analysis performed in our laboratory (Figure 27).

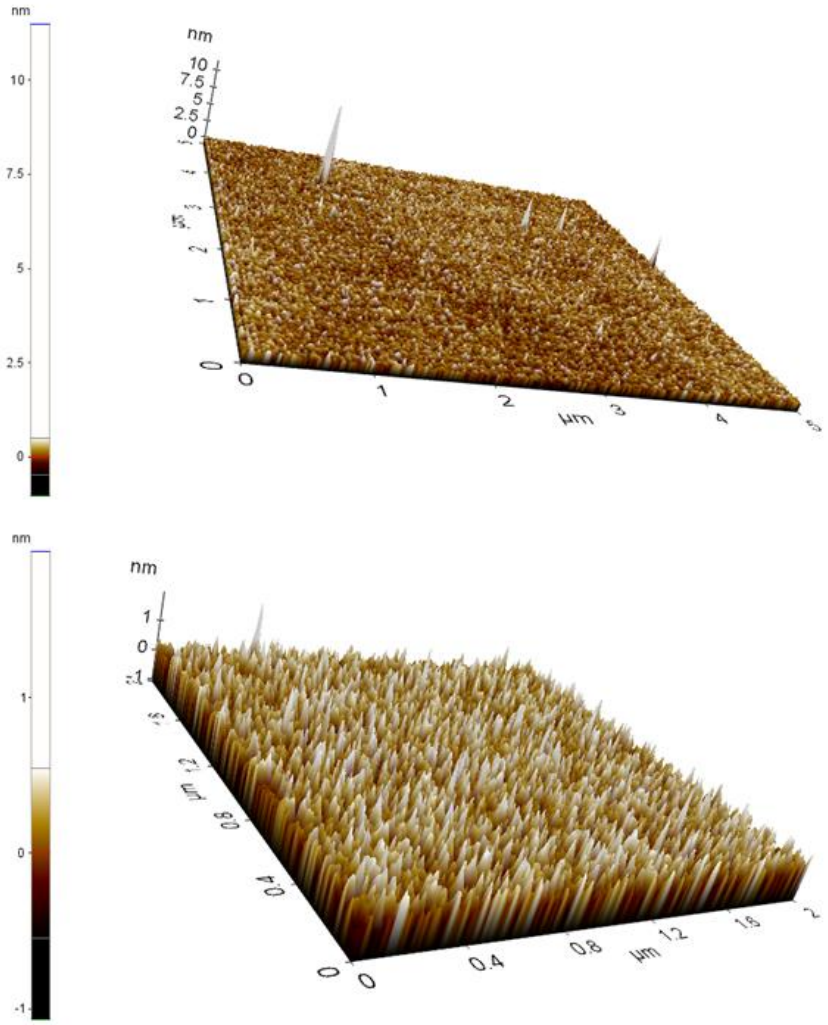

Figure 27: The image of AFM analysis on Silicon/Molybdenum ML0 sample on 5x5 microns and 2x2 microns

5.2.1 Silicon/Molybdenum multilayer ML0

In Figure 28 we show the reflectance of the multilayer coating ML0 measured around 30.4nm line. The peak of reflectance is 19,6% at 30,3nm.

The optical performances are more lower then theoretical previsions. For a good evaluation of the performances of a capping-layer, we consider this new peak value as reference for other multilayer coatings.

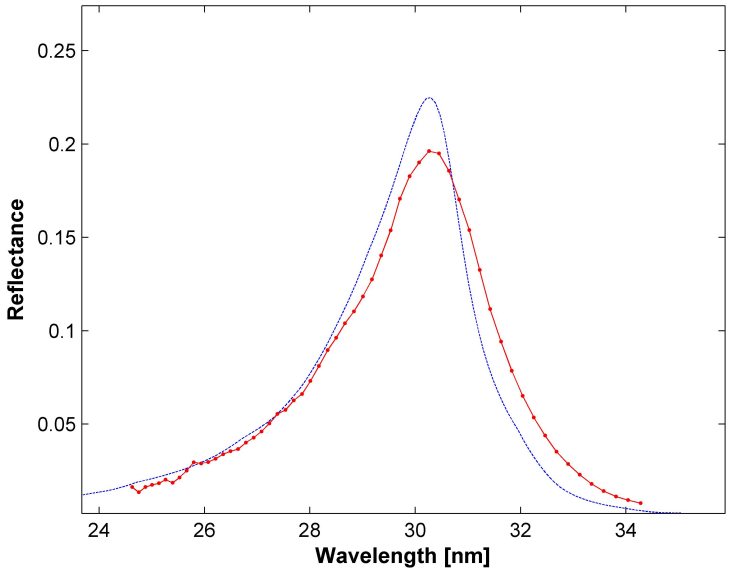

Figure 28: Comparison between the theoretical reflectance curve (dashed curve) and measured reflectance curve (interpolated curve) for ML0

5.2.2 Multilayer coatings with Iridium capping-layers

In Figure 29 we show the reflectance of the multilayer coating ML0 overcoated by Iridium/Molybdenum capping-layer CL1 measured around 30.4nm line. In this coatings a period error is observed and the reflectance peak is 25,91% at 31.64nm. The coating presents a small period error estimated by simulation around 0,2nm.

In Figure 30 we instead show the reflectance of the multilayer coating ML0 overcoated by Iridium/Silicon capping-layer CL2 measured around 30.4nm line. In this coating there is not a period error and the measured reflectance is grater than the theoretical reflectance: we have a reflectance peak of 25,95% at 30,37nm.

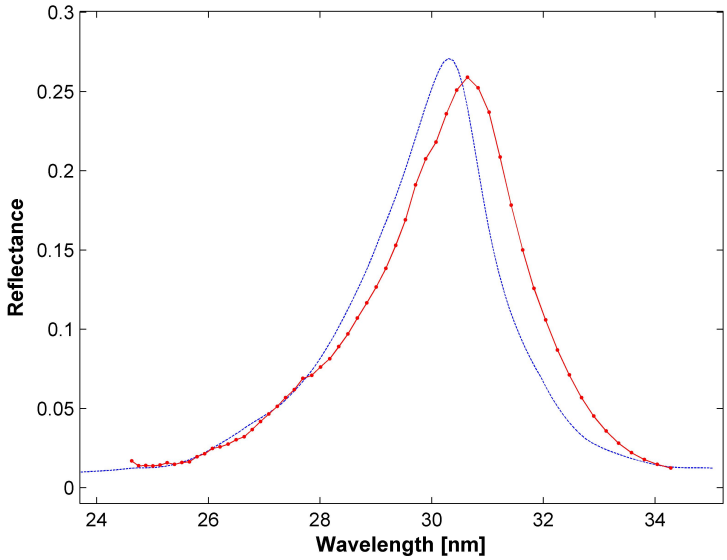

Figure 29: Comparison between the theoretical reflectance curve (dashed curve) and measured reflectance curve (interpolated curve) for ML0 overcoated by Iridium CL1

Probably, in the simulations we have foreseen a interface roughness grater.

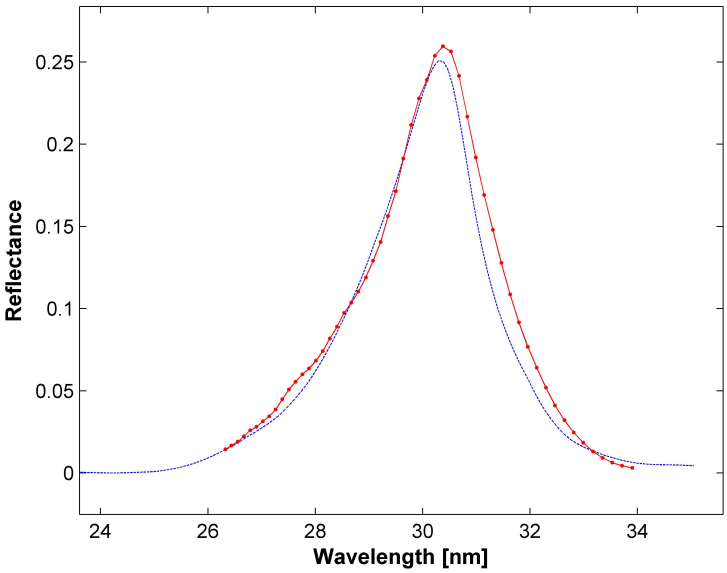

Figure 30: Comparison between the theoretical reflectance curve (dashed curve) and measured reflectance curve (interpolated curve) for ML0 overcoated by Iridium CL2

5.2.3 Multilayer coatings with Tungsten capping-layer

In Figure 31 we show the reflectance of the multilayer coating ML0 overcoated by Tungsten capping-layer CL4 measured around 30.4nm line. The reflectance peak is 21,3% at 31.37nm.

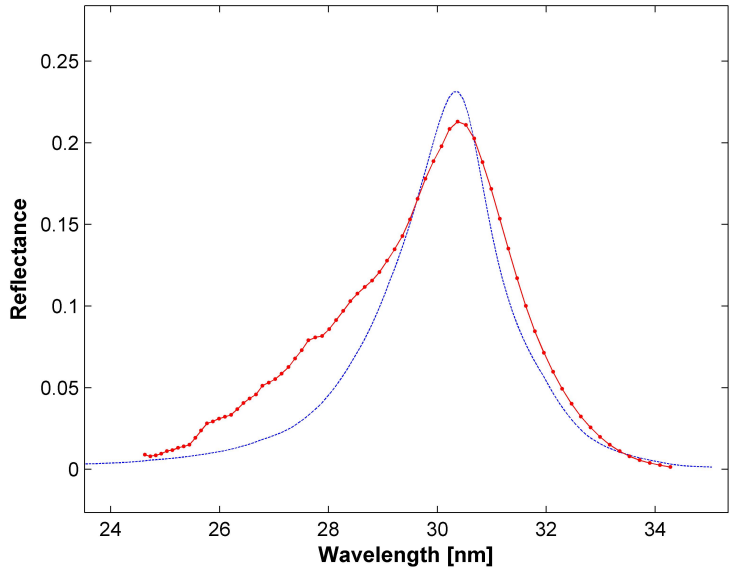

Figure 31: Comparison between the theoretical reflectance curve (dashed curve) and measured reflectance curve (interpolated curve) for ML0 overcoated by Tungsten CL4

5.2.4 Iridium/Silicon multilayer ML1 and Aluminum/Zirconium multilayer ML2

In Figure 32 we show the reflectance of the multilayer coating ML1 obtained from the Iridium and Silicon couple measured around 30.4nm line. The reflectance peak is 24% at 30.64nm: we observe that the multilayer was tunned at 30.64nm in the design phase and then there are not errors in the period length.

In Figure 33 we show the reflectance of the multilayer coating ML2 obtained from the Aluminum and Zirconium couple measured around 30.4nm line. The reflectance peak is 16,3% at 30.3nm and it is very lower than that expected from simulations: the reasons could be manifold but a good hypothesis may be the high reactivity of the Aluminum. Indeed, the Aluminum may have reacted forming new chemical species. A probable reaction may be the oxidation caused from residual oxygen in chamber during the deposition phase .

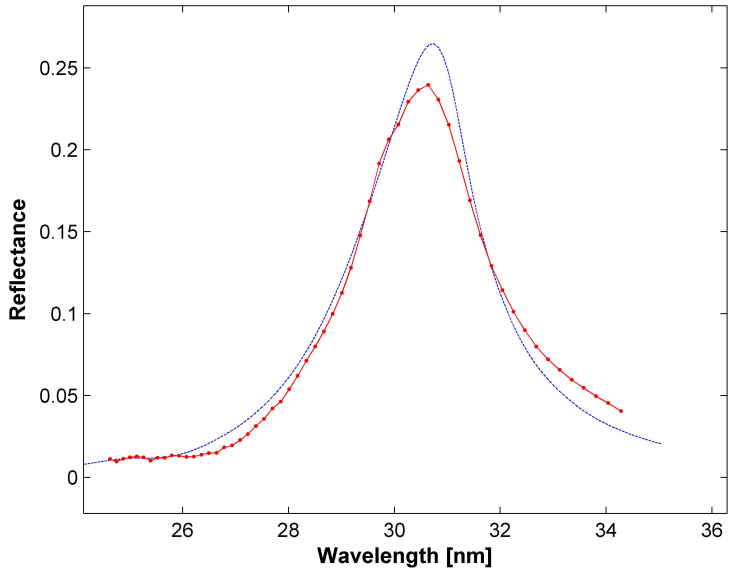

Figure 32: Comparison between the theoretical reflectance curve (dashed curve) and measured reflectance curve (interpolated curve) for Iridium/Silicon ML1

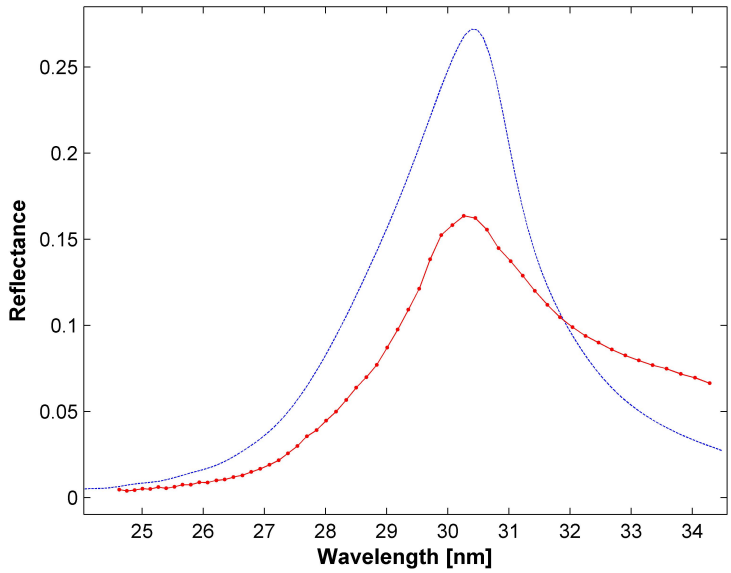

Figure 33: Comparison between the theoretical reflectance curve (dashed curve) and measured reflectance curve (interpolated curve) for Aluminum/Zirconium ML2

5.3 REFLECTANCE MEASUREMENTS AT 121,6NM LINE

The reflectance of multilayer coatings at 121,6nm line has been performed in the "Normal Incidence Facility" of the LUXOR: in Appendix A we have described in detail this facility. The 121,6nm line is obtained by Hamamatsu L7293 Deuterium lamp [13].

The reflectance has been evaluated only for a direction of the chamber in which is known the polarization index (Figure 34). The results obtained form these measurements are compared with the simulations in which we use the appropriate polarization index. However, in future the measurements will be performed also with rotated chamber in order to obtain a precise measurement of the ordinary light reflectance.

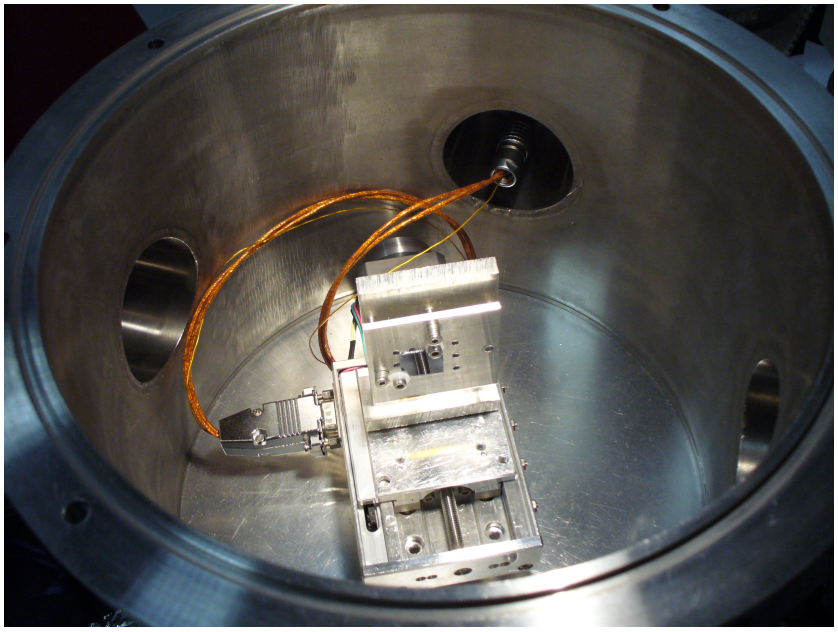

Figure 34: Samples in Normal Incidence Facility chamber.

The structure of the facility allows us only a θ-2θ measurements for different angles without operate a wavelengths scanning. The results are then fitted using IMD program using the Tarrio's constants for Molybdenum [2] in order to evaluate a possible formation of oxide on top-layer which is very critical at these wavelengths.

5.3.1 Silicon/Molybdenum multilayer ML0

In Figure 35 we show the reflectance of the multilayer coating ML0 measured at 121,6nm line. This is the only sample which has been measured also with rotated chamber: the values measured are averaged for estimating the unpolarized light reflectance.

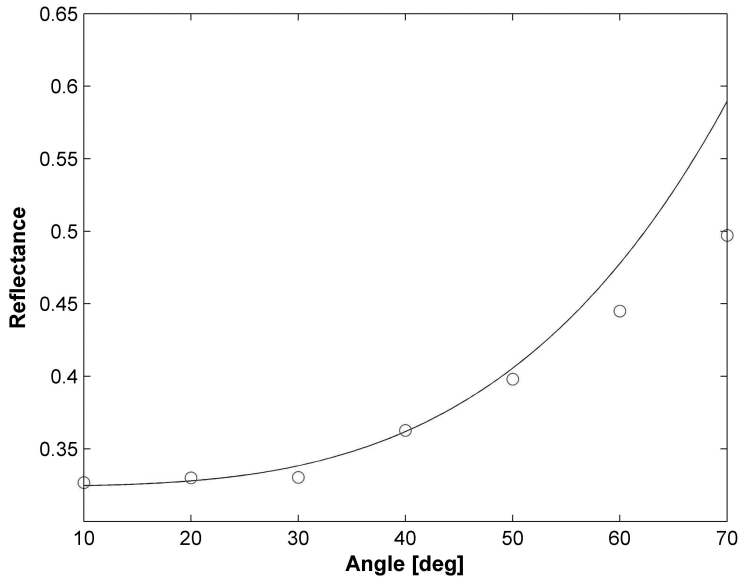

Figure 35: Theoretical (solid curve) and measured (circles) reflectance versus Angle at 121,6nm line for Molybdenum/Silicon ML0 coating

The fitting phase has shown that the oxide thickness in the topmost of the stack is around 0,7nm. Probably, this oxidation process is not concluded yet and a new measurement will be required in future.

5.3.2 Iridium capping-layers

In Figure 36 we show the reflectance of the multilayer coating ML0 overcoated by Iridium/Molybdenum capping-layer CL1 measured at 121,6nm line and compared with a simulations performed by IMD.

In Figure 37 we instead show the reflectance for Iridium/Silicon capping-layer CL2.

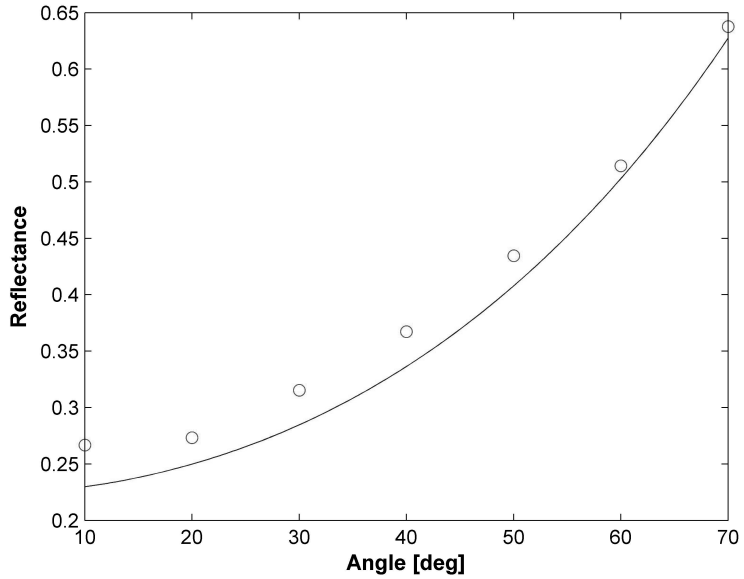

Figure 36: Theoretical (solid curve) and measured (circles) reflectance versus angle at 121,6nm line for ML0 overcoated by Iridium/Molybdenum capping-layer CL1

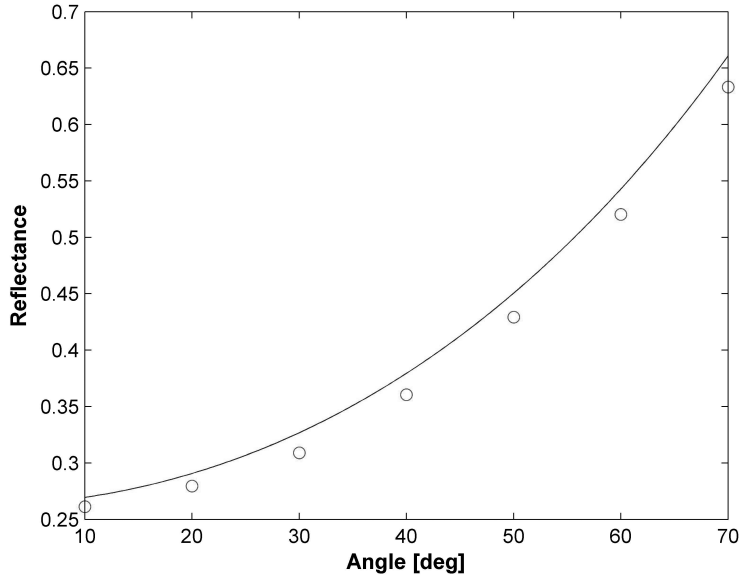

Figure 37: Theoretical (solid curve) and measured (circles) reflectance versus angle at 121,6nm line for ML0 overcoated by Iridium/Silicon capping-layer CL2

5.3.3 Tungsten capping-layer

In Figure 38 we show the reflectance versus angle of the multilayer coating ML0 overcoated by Tungsten capping-layer CL4 measured at 121,6nm line.

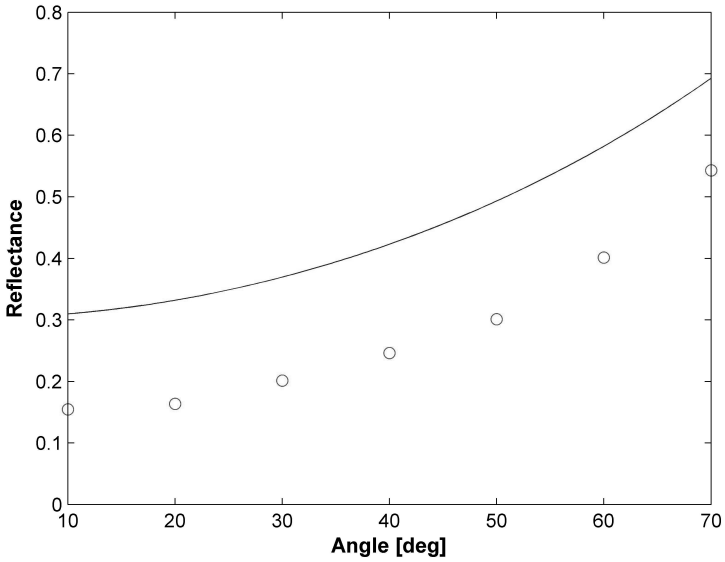

Figure 38: Theoretical (solid curve) and measured (circles) reflectance versus angle at 121,6nm line for ML0 overcoated by Tungsten capping-layer CL4

We can observe a big difference between theoretical and experimental reflectance: such deviation may be caused by the presence of oxide in the top of the stack. From this preliminary analysis seems that also Tungsten oxidizes very much, contrary to our predictions; unfortunately, the optical constants of this oxide are not available at these wavelengths and we can't estimate the thickness of this oxide layer.

5.3.4 Iridium/Silicon multilayer ML1 and Aluminum/Zirconium multilayer ML2

In Figure 39 we show the reflectance versus angle of the Iridium/Silicon multilayer coating ML1 measured at 121,6nm line.

In Figure 40 we show the reflectance versus angle of the Aluminum/Zirconium multilayer coating ML2 measured at 121,6nm line.

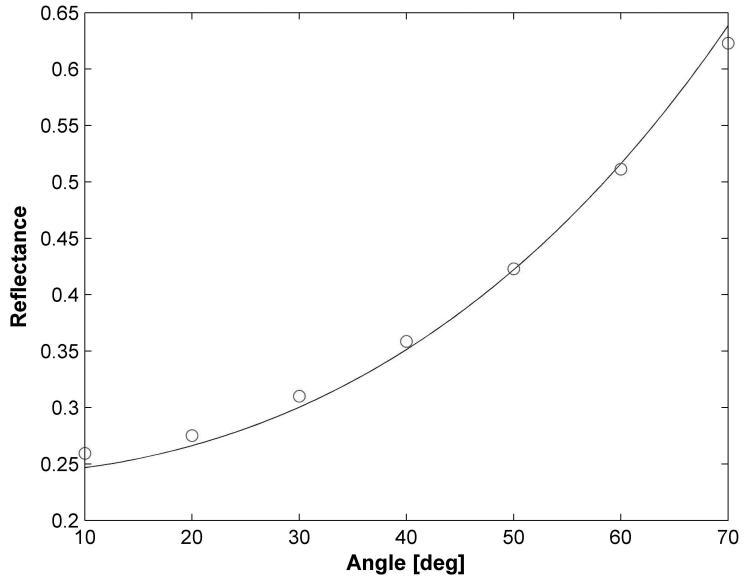

Figure 39: Theoretical (solid curve) and measured (circles) reflectance versus angle at 121,6nm line for Iridium/Silicon multilayer ML1

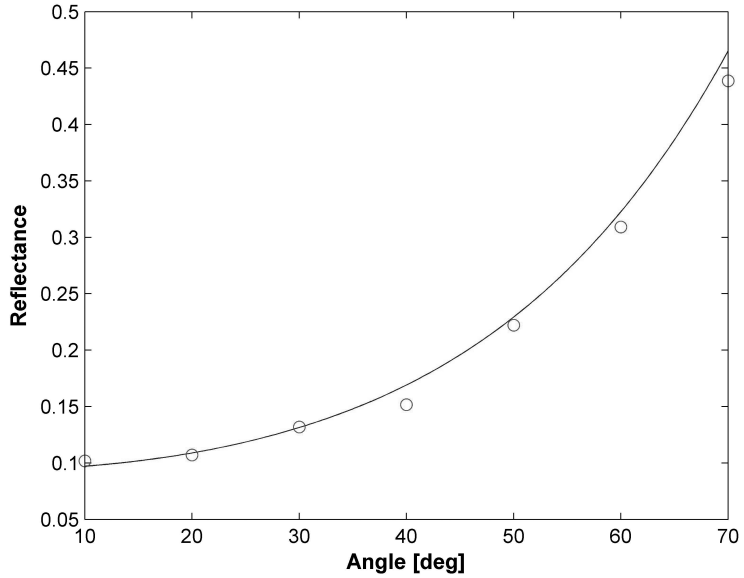

Figure 40: Theoretical (solid curve) and measured (circles) reflectance versus angle at 121,6nm line for Aluminum/Zirconium multilayer ML2

Aluminum is a metal very reactive and it is interesting estimate how much it oxidizes; the most probable native oxide is Al_2O_3 and fortunately its optical constants are available. From a fitting of the experimental data we have found an Aluminum oxidation in top-layer around 2nm.

5.4 REFLECTANCE MEASUREMENTS IN THE VISIBLE WAVELENGTHS

Reflectance at visible wavelengths of the multilayer coatings is performed by the Varian UV-Vis-NIR spectrophotometer "Cary 5000" [35]. The total reflectance[1] is measured using an integrating sphere which performs the measure at 8 degrees of incidence; the geometry of the integrated sphere allows us to measure also only the stray light and then we can compute the specular reflectance. A polarizer at the entrance of the integrating sphere is used for ensuring the measurements of the samples in s-condition and p-condition: the ordinary light reflectance is still estimated with the average of the two polarized components.

The spectrophotometer has a deuterium lamp and an halogen lamp with a monochromator which selects the desired wavelength: the system allows a scan in UV, Visible and Infrared range. In our analysis, we have performed the measurements from 400nm up to 800nm and here we present the results (from Figure 41 up to Figure 46).

All films have a good reflectance and always is greater than simulations. The highest optical performances at these wavelengths are obtained with the Aluminum/Zirconium coating caused from the hight reflectivity of the Aluminum.
Iridium capping-layers and Iridium multilayer film increase the reflectance respect on classical Mo/Si film while the Tungsten capping-layer doesn't adds substantial benefits.

1 The total reflectance is the superposition of the specular reflectance and the stray light reflectance

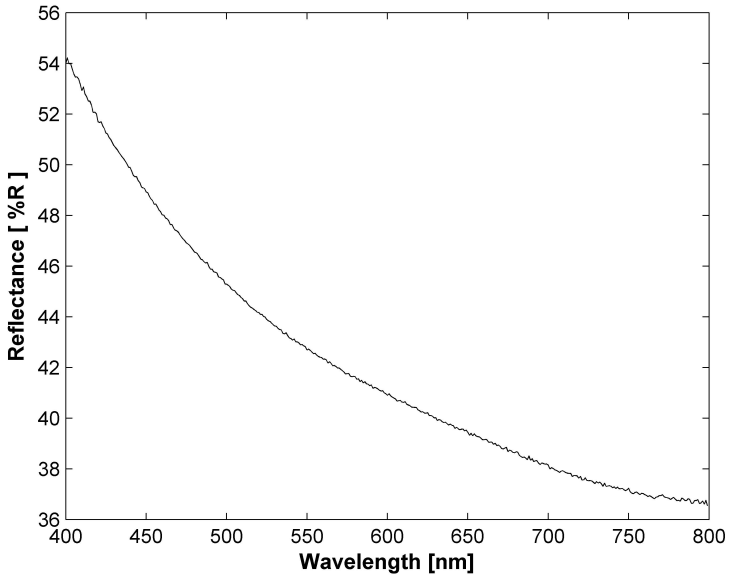

Figure 41: Reflectance in visible wavelengths for Silicon/Molybdenum multilayer ML0

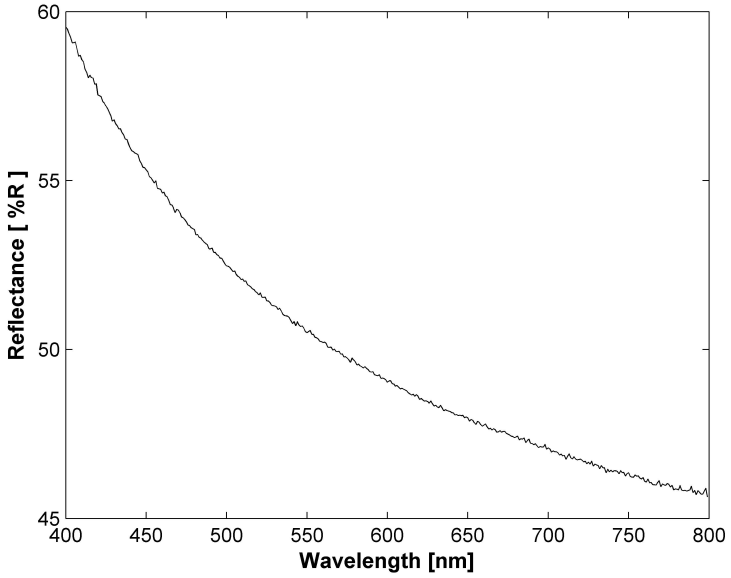

Figure 42: Reflectance in visible wavelengths for Silicon/Molybdenum multilayer with Iridium/Silicon capping-layer CL1

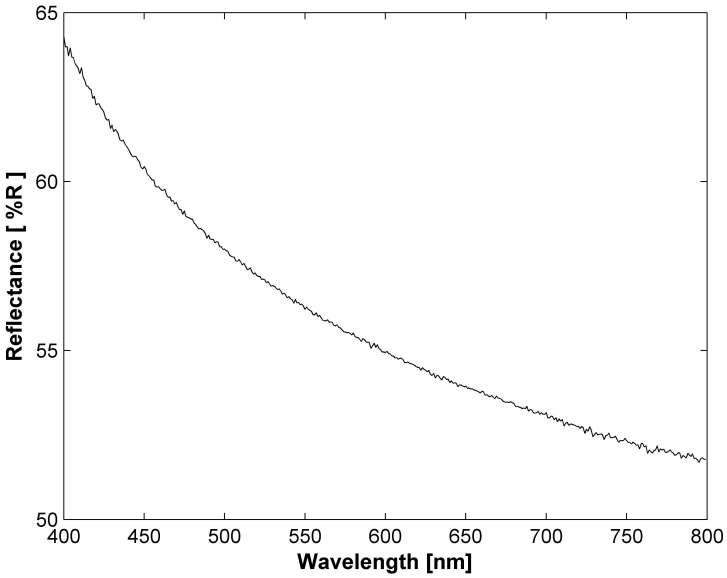

Figure 43: Reflectance in visible wavelengths for Silicon/Molybdenum multilayer with Iridium/Molybdenum capping-layer CL2

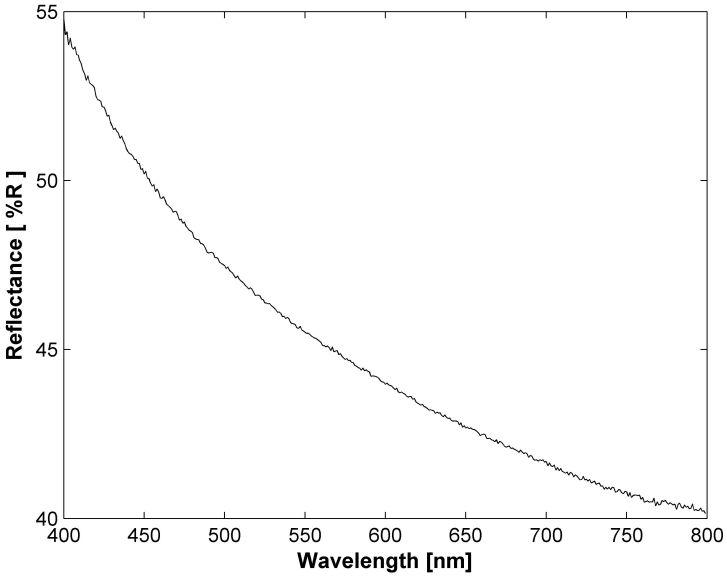

Figure 44: Reflectance in visible wavelengths for Silicon/Molybdenum multilayer with Tungsten capping-layer CL4

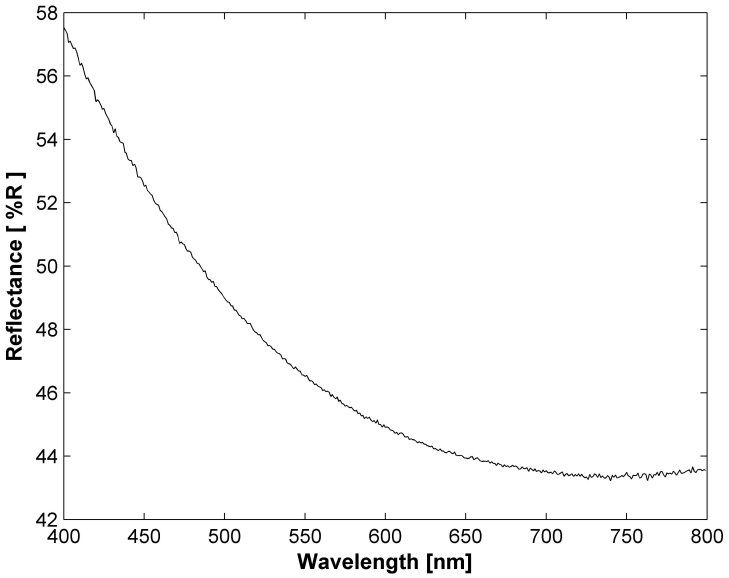

Figure 45: Reflectance in visible wavelengths for Iridium/Silicon multilayer ML1

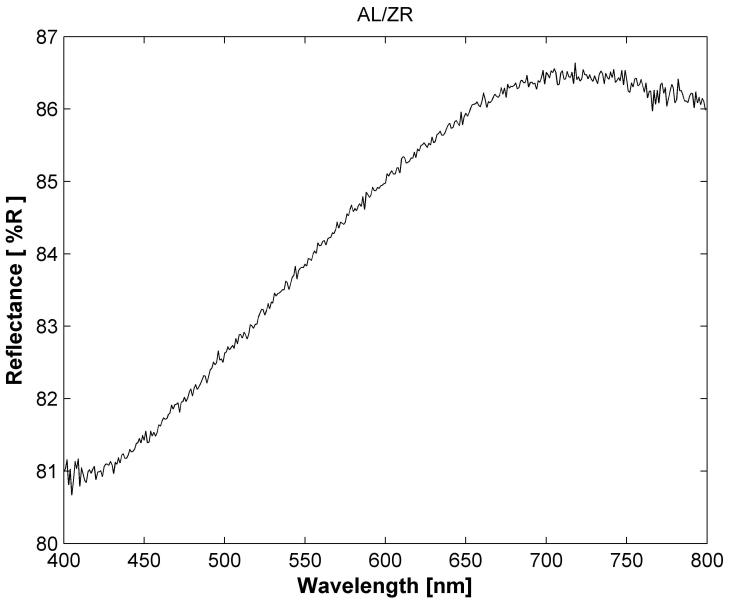

Figure 46: Reflectance in visible wavelengths for Aluminum/Zirconium multilayer ML2

6 CONCLUSIONS

In this work we have designed and tested new multilayer coatings for the mirrors inside the chronagraph METIS which will be on board of Solar Orbiter mission planned by ESA.

The early experimental results

Early reflectance measurements have already identified the coatings which are indicated for our purposes. The Iridium capping-layers have shown hight reflectance at 30,4nm line in according to theoretical simulations. The topmost layers doesn't oxidize and the good reflectance at 121,6nm line is also guaranteed. Furthermore, the Iridium reflects very well the visible light and so we have a good mirror also in the visible range. The stability seems good but we must check again in future for ensuring this aspect. The remarks made for the Iridium capping-layers are still valid for the innovative multilayer coatings based on Iridium/Silicon couple. The best optical performances are obtained by a Silicon/Molybdenum overcoated by a Iridium/Silicon capping layer which reflects the 26% at 30,4nm, the 25% at 121,6nm and the 48% at 600nm.

Tungsten capping-layer is instead disappointing because, even if it has a moderate reflectance at 30,4nm line, the reflectance at 121,6nm is very low. Probably the Tungsten oxidizes but we can't investigate this point because the optical constants of this oxide are not available in this moments.
Finally, Aluminum/Zirconium multilayer coating has proved low reflectance at 30,4nm and 121,6nm: with our analysis it's not easy understand the behavior of this multilayer film which is very different from the simulations and further investigations should be performed.
In future, we will make also the coating with Ruthenium capping-layer and we will evaluate its optical performances.

The next testing phase

Now, the samples measured are stored in standard pressure and temperature condition and will be measured again after one year for evaluating the aging. The remaining samples will be tested for evaluating the thermal and particles bombardments stability: the experiments must simulate as well as possible the real conditions which the multilayer coatings will support during the mission and only after these experimentations we can chose the effective film which will fly toward the Sun.

A EUV NORMAL INCIDENCE FACILITY OF LUXOR

The early reflectance measurements at HI Lyman-α line are performed in LUXOR laboratory in Padova (Italy). These wavelengths do not propagate in the normal ambiance because the air becomes absorbent and then a specific facility is required: in the measurements we have used the facility shown in Figure 47 named "Normal Incidence Facility".

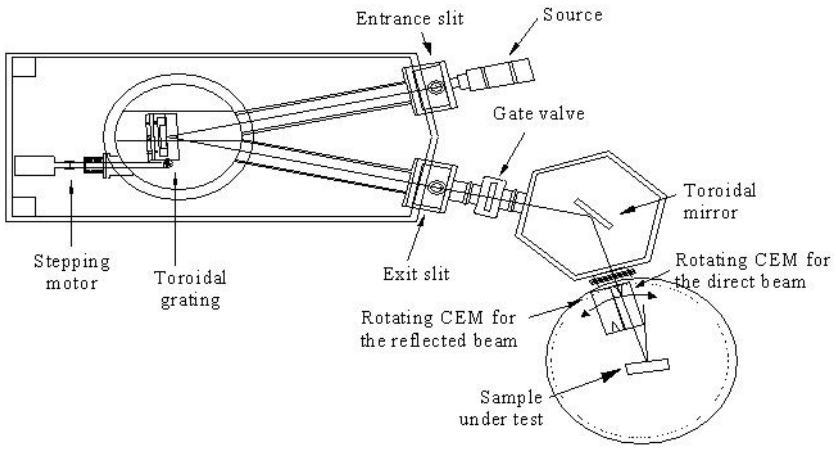

Figure 47: Scheme of the Normal Incidence Facility of LUXOR in Padova

This facility is used in the spectral range between around 30nm up to 160nm and its name results from the grating mounting which is almost normal to source. The first optical element is a monochromator which is obtained with a toroidal grating overcoated by Platinum with 600grooves/mm. The radius of curvature of the grating is $0,5$m and the subtended angle between incident and refracted light is 25°. In order to control the band of the optical system, there are two slits, one just after the source (input slit) and one after the grating (output slit): for obtaining a stigmatic system the slits are in two points of the Rowland's circle. The height of the slits is 3mm and the width is adjustable from 0 to 650μm by a micrometer.
A step by step engine moves the monochromator for selecting the desired wavelengths. We note that when the grating rolls its

Rowland's circle rolls and the slits exit from the circle. In order to reduce the aberration in these cases, the grating is rolled and contemporaneously moved along a circumference centered in a third point C which is not in Rowland's circle: the point C is chosen in order to obtain a rotation of the grating surface along the This monochromator is said "in Johnson-Onaka configuration".

After the output slit, a gate valve can isolate the monochromator chamber from the following hexagonal chamber in which is placed a toroidal mirror overcoated by platinum. This mirror focuses the light from the output slit in the center of the measuring chamber.

The samples are placed in a support which runs along a sled fixed to bottom of chamber by a rotating graduated mechanism. Also in the lid of the chamber there is a rotating graduated mechanism which is used for placing CEM detector: this facility allows us to performing reflectance measurements in $\theta - 2\theta$ configuration varying the incidence angle.

The multiple reflections in optical layout inside the facility polarize the light used in the measurements. This polarization depends on wavelengths because the Platinum in the mirrors changes its behavior (or, more precisely, its optical constants). We describe the polarization of the facility using the parameter f defined as

$$f = \frac{I_s - I_p}{I_s + I_p}$$

Parameter f has been measured and it is available in the range in which the facility works: in our measurements, only the 121.6nm wavelength is used and in these conditions $f = 0,89$.

The output slit creates a differential pressure between monochromator chamber and measuring chamber. In order to achieve a good vacuum in both chambers the vacuum system is divided in two parts: a vacuum system for monochromator chamber and a vacuum system for the measuring chambers. Low vacuum in both parts is achieved by a scroll pump which is connected with two different valves. The high vacuum is instead achieved by two turbo-molecular pumps, one for monochromator and one for measuring chamber, connected by two slide valves: the vacuum achieved in the chambers is around 10^{-6}mbar.

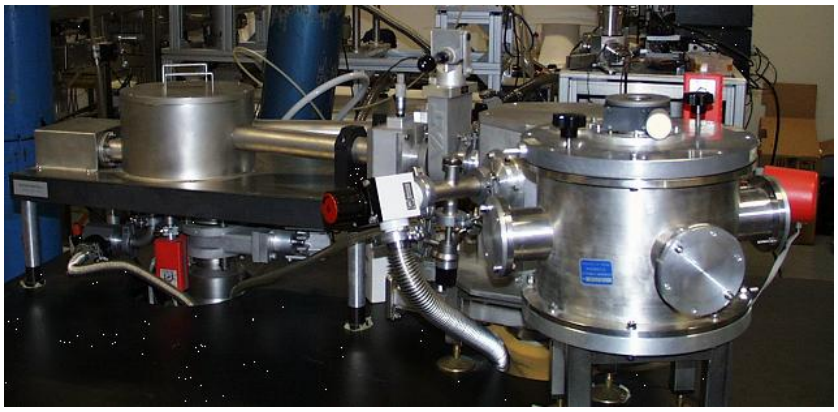

Figure 48: An image of Normal Incidence Facility

BIBLIOGRAPHY

[1] A. L. Aquila. *Development of extreme ultraviolet and soft x-ray multilayer optics for scientific studies with femtosecond/attosecond sources*. PhD thesis, 2009.

[2] T. B. Lucatorto J. M. Slaughter C. Tarrio, R. N. Watts and C. M. Falco. Optical constants of in situ deposited films of important extreme-ultraviolet multilayer mirror materials. *APPLIED OPTICS*, 37:4100 – 4104, 1998.

[3] Palik E. D. *Handbook of Optical Constants of Solid III*. Academic Press, 1998. ISBN 0-12-544423-0.

[4] Brunaud J. et al. Delaboudiniere J.P., Artzner G.E. Extreme-ultraviolet imaging telescope for the soho mission. *Solar Physics*, 162:291–312, 1995.

[5] Gullikson E. *X-Ray Interactions With Matter - Optical Constants*. http://henke.lbl.gov/optical_constants/, 1993.

[6] Banse T. Saito K. Kondo Y. Ichimaru S.-Takenaka H. Ejima T., Yamazaki A. Aging and thermal stability of mg/sic and mg/y203 reflection multilayers in the 25-35 nm region. *APPLIED OPTICS*, 44:5446 – 5453, 2005.

[7] ESA. *Solar Orbiter Hompage*. http://sci.esa.int/science-e/www/area/index.cfm?fareaid=45.

[8] ESA. *Solar Orbiter Payload Definition Document*, 2007.

[9] ESA. *Solar Orbiter environmental specification*, 2008.

[10] BIRA-LABS ESA. *Space Environment Information System*. http://www.spenvis.oma.be/spenvis/.

[11] NASA ESA. *The SOHO Extreme ultraviolet Imaging Telescope*. http://umbra.nascom.nasa.gov/eit/.

[12] Liu Shi-Jie Wang Xiao-Guang Chen Bo Fan Xian-HongLi Min, Ni Qi-Liang. Change of reflectivity of mo/si multilayer irradiated by proton. *ACTA PHYSICA SINICA*, 57:6494–6499, 2008.

[13] Hamamatsu. *Datasheet of Deuterium Lamp L7293*. http://sales.hamamatsu.com/assets/pdf/catsandguides/L2D2_TLSO1027E08.pdf.

[14] B.N. Handy. The transition region for coronal explorer. *Solar Physics*, 187:229, 1999.

[15] Tadayuki Ohchi-E.M. Gullikson Hisataka Takenaka, Satoshi Ichimaru. Soft-x-ray reflectivity and heat resistance of sic/mg multilayer. *JOURNAL OF ELECTRON SPECTROSCOPY AND RELATED PHENOMENA*, 144:1047 – 1049, 2005.

[16] Ted D. Tarbella et al. Jean-Pierre Wülser, James R. Lemena. Euvi: the stereo-secchi extreme ultraviolet imager. *Proc. SPIE*, 5171:111–122, 2004.

[17] et al. Jingtao Zhu, Zhanshan Wang. High reflectivity multilayer for he-ii radiation at 30.4nm. *Applied Optics*, 47, 2008.

[18] Benbalagh R. Maury H. Andre JM. Dankhazi Z.-Rolland G. Jonnard P., Jarrige I. Physico-chemical and x-ray optical characterizations of a mo/si multilayer interferential mirror upon annealing. *SURFACE SCIENCE*, 589:164 – 172, 2005.

[19] Windt D. L. Imd: software for modeling the optical properties of multilayer films. *Computer Physics*, 12:360–370, 1998.

[20] Singh M. and Braat J. J. M. Capping layers for extreme-ultraviolet multilayer interface coatings. *Optics Letters*, pages 259 – 261, 2001.

[21] E. Wolf M. Born. *Principles of Optics*. Pergamon Press, 6th edition, 1980.

[22] D. L. Windt G. Monaco P. Nicolosi M. G. Pelizzo, M. Suman. Innovative methods for optimization and characterization of multilayer coatings. *EUV and X-Ray Optics: Synergy between Laboratory and Space, René Hudec; Ladislav Pina, Editors, 73600Q*, 7360:360–370, 2009.

[23] D. L. Windt P.Nicolosi M. Suman, M. G. Pelizzo. Euv multilayer coatings with high spectral purity for solar imaging. *Applied Optics*, 49(Issue 29):5432–5437, 2009.

[24] Jonnard P. Le Guen K. Andre J. M. Wang Z.-Zhu J. Dong J. Zhang Z. Bridou F. Delmotte F. Hecquet C. Mahne N. Giglia A. Nannarone S. Maury, H. Thermal cycles, interface chemistry and optical performance of mg/sic multilayers. *EUROPEAN PHYSICAL JOURNAL B*, 64:193 – 199, 2008.

[25] NASA. *Transition Region and Coronal Explorer*. http://trace.lmsal.com/.

[26] M. Suman D. Windt P. Nicolosi, M.G. Pelizzo. a-periodic multilayer structures for euv lithography. Technical report, PCT/EP2007/060477, University of Padova, CNR-INFM, RXOLLC (N.Y. USA), 2007.

[27] Monaco G. Nicolosi P. D. L. Windt Pelizzo M.G., Suman M. High performance euv multilayer structures insensitive to capping layer optical parameters. optics express. *Optics express*, 16(19):15228–15237, 2008.

[28] Song X. Z. Jerome A. Delmotte F.-Mercier R. Bougnet M. Bouyries P. Ravet M.-F., Bridou F. and J.-P. Delaboudiniere. Ion beam deposited mo/si multilayers for euv imaging applications in astrophysics. *Proc. SPIE*, 5250:99–108, 2004.

[29] D. L.; Winter B.; Harra L.; Lamoureux H.; Eriksson F. Rousseau, A. D.; Windt. Stability of euv multilayers to long-term heating, and to energetic protons and neutrons, for extreme solar missions. *Proc. SPIE*, 5900:164–172, 2005.

[30] M.G. Pelizzo P. Nicolosi S. Fineschi D. Windt S. Zuccon, D. Garoli. Multilayer coatings for multiband spectral observations. *ESTEC, Noordwijk, The Netherlands*, June 2006.

[31] Eberhard Spiller. *Soft X-Ray optics*. SPIE Optical Engineering Press, 1th edition, 1994.

[32] D. G. Stearns. *Aplicated Physics*, 6:491, 1989.

[33] M. Suman. *Studio dell'interazione della radiazione elettromagnetica con strutture nanometriche per lo sviluppo di ottiche*. PhD thesis, 2008.

[34] Electra (Trieste). *Bending magnet for Emission Absorption and Reflectivity beamline*. http://www.elettra.trieste.it/experiments/beamlines/bear/index.html.

[35] Varian. *Cary 5000 UV-Vis-NIR spectrophotometer*. http://www.varianinc.com/cgi-bin/nav?products/spectr/uv/cary5000/cary_5000.

[36] D. L. Windt and W. K. Waskiewicz. Multilayer facilities required for extreme-ultraviolet lithography. *J. Vac. Sci. Technol. B*, 12:3826 – 3832, 1994.

[37] Seely J. Windt D. L., Donguy S. and B. Kjornrattanawanich. Experimental comparison of extreme-ultraviolet multilayers for solar physics. *Applied Optics*, 43:1835–1848, 2004.